SUB-WAVELENGTH RESOLUTION IN A PHOTONIC CRYSTAL SUPERLENS

A THESIS

SUBMITTED TO THE DEPARTMENT OF PHYSICS

AND THE INSTITUTE OF ENGINEERING AND SCIENCE

OF BİLKENT UNIVERSITY

IN PARTIAL FULFILLMENT OF THE REQUIREMENTS

FOR THE DEGREE OF

MASTER OF SCIENCE

By

Ertuğrul Çubukçu

July, 2003

I certify that I have read this thesis and that in my opinion it is fully adequate, in scope and in quality, as a thesis for the degree of Master of Science.

Prof. Dr. Ekmel Özbay (Advisor)

I certify that I have read this thesis and that in my opinion it is fully adequate, in scope and in quality, as a thesis for the degree of Master of Science.

Assist. Prof. Dr. Ceyhun Bulutay

I certify that I have read this thesis and that in my opinion it is fully adequate, in scope and in quality, as a thesis for the degree of Master of Science.

Assoc. Prof. Dr. Levent Gürel

Approved for the Institute of Engineering and Science:

Prof. Dr. Mehmet B. Baray
Director of the Institute

ABSTRACT

SUB-WAVELENGTH RESOLUTION IN A PHOTONIC CRYSTAL SUPERLENS

Ertuğrul Çubukçu
M.S. in Physics
Supervisor: Prof. Dr. Ekmel Özbay
July, 2003

Materials that can bend light in the opposite direction to normal ('left-handed' materials) reverse the way in which refraction usually works-this negative refractive index is due to simultaneously negative permeability and permittivity. Here we demonstrate negative refraction of electromagnetic waves in a two-dimensional dielectric photonic crystal that has a periodically modulated positive permeability and a permeability of unity. This experimental verification of negative refraction is a step towards the realization of a 'superlens' that will be able to focus features smaller than the wavelength of light. Our structure consists of a square array of alumina rods in air. To obtain the frequency range within which the negative refraction and the other peculiar properties incorporated with it, we have calculated the the equal frequency contours of our photonic crystal with the photonic plane wave expansion method. We found out that 13.7 GHz is the optimum frequency for negative refraction. We took transmission measurements to confirm our structure's predicted negative refraction: we used the the interfaces of the photonic crystal in the $\Gamma - M$ direction. Our experiments were simulated with the finite-difference time-domain method (FDTD). The negative index of refraction was determined to be -1.94, which is close to the theoretical value of -2.06 calculated by the FDTD method. Since we know that we have a negative refractive material , we used our crystal to test the superlensing effect that was predicted for negative refractive materials. We have demonstrated that the image of two coherent point sources separated by a distance of $\lambda/3$ can be resolved. We have extended our approach to the case with two incoherent point sources, and we have achieved subwavelength resolution for this configuration as well. To our knowledge, this is the first demonstration of subwavelength resolution of electromagnetic waves in a negative index material.

Keywords: Photonic Crystals, Left-Handed Material, Negative-Refractive Material, Negative Refraction, Superlens, Subwavelength Resolution, Photonic Band Structure, Equal Frequency Contours.

ÖZET

FOTONIK KRISTAL BIR SUPERLENSTE DALGABOYU-ALTI COZUNURLUK

Ertuğrul Çubukçu
Fizik, Yüksek Lisans
Tez Yöneticisi: Prof. Dr. Ekmel Ozbay
Temmuz, 2003

Mikrodalga bölgesinde çalışan iki boyutlu bir fotonik kristalin değerlik bandındaki bir frekans için tekli negatif kırınımı ve süperlens etkisini deneysel ve teorik olarak gösterdik. Fotonik kristalden kırılan elekromanyetik dalgaları ölçerek kırılma indisini teorik değeri olan -2.06'ya çok yakın olan -1.94 olarak bulduk. Geçirgenlik taraması ölçümü tekniği kullanılarak bir noktasal kaynaktan yayılan odaklanmış elektromanyetik dalgaların uzaydaki güç dağılımı ölçüldü. Odaklanan demetin uzaydaki maksimunun yarısında tam genişliği, zamanda sonlu fark (FDTD) metodu simülasyonlarıyla iyi uyum içerisinde olan, 0.33λ olarak ölçüldü. Ayrıca birbirlerinden $\lambda/3$ kadar uzakta olan iki noktasal kaynağın görüntüsünün bizim süperlensimiz kullanılarak dalgaboyu altı çözülebildiğini gösterdik.

Anahtar sözcükler: Fotonik Kristal, Solak Materyal, Negatif Materyal, Negatif Kırılma, Fotonik Bant Yapısı, Eş Frekans Kontürü.

Acknowledgement

I would like to express my gratitude to my thesis supervisor Prof. Ekmel Özbay for his invaluable guidance and motivation during the past three years. I'd like to thank Dr. Mehmet Bayindir for helping me with everything. I am also grateful to the members of our department, and especially to Emine Abla.

Contents

List of Figures

List of Tables

Chapter 1

Introduction

It is a well-known fact that allowed and forbidden energy bands for electrons in a semiconductor do not depend on the properties which are specific for electrons or for the atoms in the crystal. The reason for the formation of these gaps is nothing but scattering of electrons from a periodic potential. Due to Bragg reflections [1] from these periodic structures, electrons having certain energies are forbidden to propagate through crystal in certain directions (Fig. 1.1). If the gap extends to all possible directions then this is called complete band gap. For example, the gap between valence and conduction bands of a semiconductor is a complete band gap.

An analogous situation arise for electromagnetic waves propagating through a material medium with a periodic variation in the dielectric constant. Such kind of materials are called photonic band gap (PBG) materials or photonic crystals. So, it can be understood that PBG structures can be designed by the periodic variation of the dielectric constant of the medium in either one, two or three dimensions. Due to this periodic structure, electromagnetic waves cannot propagate inside the photonic crystal for certain frequency ranges in all directions. The photonic band structure of a photonic crystal depends on the crystal structure, lattice constant, geometry, dielectric constants of materials, and the filling fraction (volume occupied by material divided by total volume of the crystal).

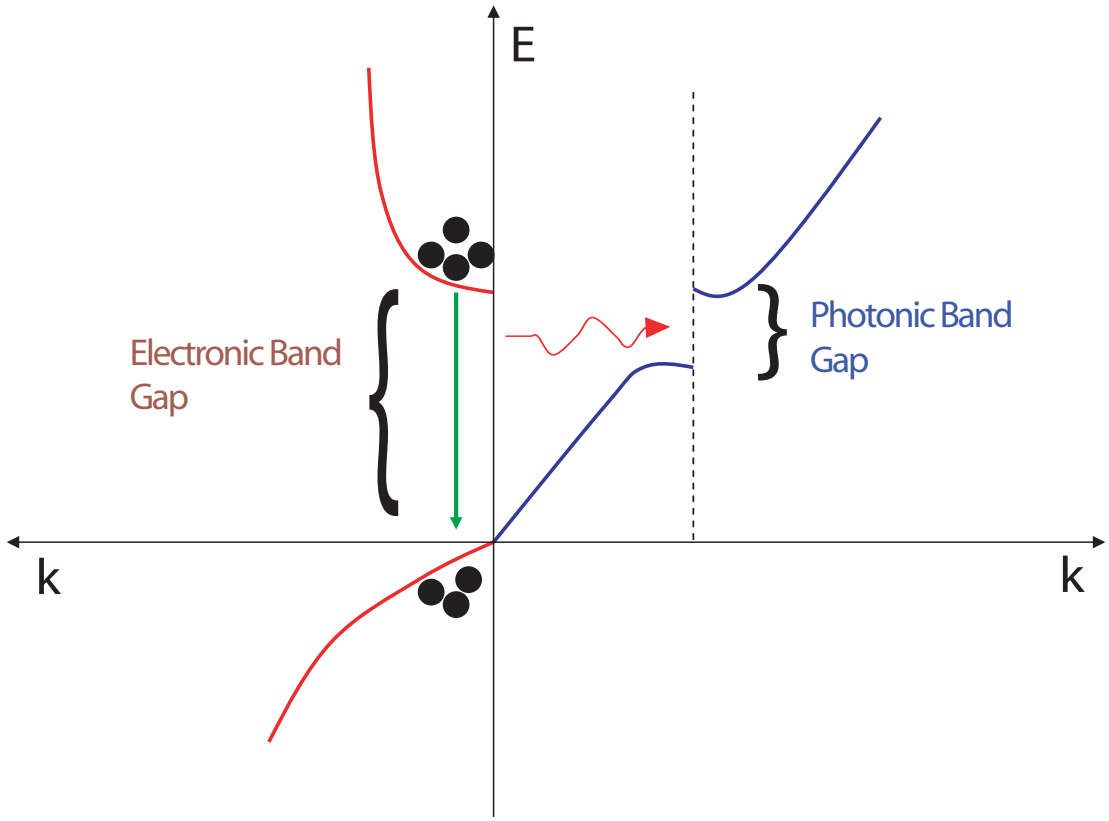

Figure 1.1: Schematics of photonic and electronic band gaps.

The existence of photonic band gap was first predicted by Yablonovitch [2] and John [3] in late 80's. In principle demonstration of the photonic band gap seems to be straightforward, but it took five years until it was experimentally demonstrated by Yablonovitch and his co-workers [4]. This first three-dimensional (3D) photonic crystal, called as Yablonovite, was built by placing a triangular mask of holes over the dielectric host and drilling through each hole three times at an angle of 35.26° away from the normal and spread out 120° on the azimuthal directions. Of course, this was not the only way for building a photonic crystal. Then, Iowa State group demonstrated experimentally the first layer-by-layer dielectric photonic crystal [5, 6, 7]. The layer-by-layer photonic crystal is the first structure that was fabricated at optical frequencies [8, 9, 10].

The existence of full photonic band gaps in PBG materials has important potential applications in the area of quantum optics and laser technology. Waveguiding in photonic crystals is one of the most important applications. The waveguiding effect in photonic crystals was first demonstrated both theoretically and experimentally by MIT group [11, 12]. It was a two dimensional one and built by creating planar defects in the perfect crystal. But this type of waveguides were not efficient enough. Then, Bilkent photonic band gap group demonstrated a new waveguiding mechanism [13, 14, 15]. This type of waveguides are called coupled-cavity waveguides (CCWs) after the demonstration of Bilkent group. Transmissions as high as 100% can be observed in CCWs. All of the above applications make use of the existence of the photonic band gap. Recently, it is realized that photonic crystals can be used as super-refractive materials by the virtue of the richness of their band structure. In this thesis, we investigate the refractive properties of two-dimensional photonic crystals.

Chapter 2

Theory of photonic crystals

Even we have electromagnetic wave propagation in a photonic crystal, we can analyze this system in the light of the Maxwell equations. The four macroscopic Maxwell equations [16], which are valid for any electromagnetic system in cgs units are

$$\nabla \cdot \mathbf{B} = 0 \,, \tag{2.1}$$

$$\nabla \times \mathbf{E} + \frac{1}{c}\frac{\partial \mathbf{B}}{\partial t} = 0 \,, \tag{2.2}$$

$$\nabla \cdot \mathbf{D} = 4\pi\rho \,, \tag{2.3}$$

$$\nabla \times \mathbf{H} - \frac{1}{c}\frac{\partial \mathbf{D}}{\partial t} = \frac{4\pi}{c}\mathbf{J} \,. \tag{2.4}$$

Here $\mathbf{E}$ and $\mathbf{B}$ are the macroscopic electric and magnetic fields, respectively. $\mathbf{D}$ is the displacement field and $\mathbf{H}$ is the magnetic induction field. $\mathbf{J}$ and ρ are the free current and charge densities, respectively. In this study, we will restrict ourselves to propagation in medium having a spatially changing dielectric permittivity and

no free charges or currents. So, we could assume that $\mathbf{J} = 0$ and $\rho = 0$. Then we have to relate $\mathbf{E}$ to $\mathbf{D}$, and $\mathbf{B}$ to $\mathbf{H}$ with the constitutive relations of our problem. Since, we are allways working with the small field strengths, we don't have to bother with the nonlinearity involved in the system [17]. Thus, the constitutive relations turn out to be

$$\mathbf{D}(\mathbf{r}) = \varepsilon(\mathbf{r})\mathbf{E}(\mathbf{r}) \ , \tag{2.5}$$

$$\mathbf{B}(\mathbf{r}) = \mu(\mathbf{r})\mathbf{H}(\mathbf{r}) \ . \tag{2.6}$$

The magnetic constitutive relation reduces to $\mathbf{B}(\mathbf{r}) = \mathbf{H}(\mathbf{r})$ for our nonmagnetic system. Now, with all of this initial realistic assumptions, the Maxwell equations become

$$\nabla \cdot \mathbf{H}(\mathbf{r}, t) = 0 \ , \tag{2.7}$$

$$\nabla \times \mathbf{E}(\mathbf{r}, t) + \frac{1}{c}\frac{\partial \mathbf{H}(\mathbf{r}, t)}{\partial t} = 0 \ , \tag{2.8}$$

$$\nabla \cdot \varepsilon(\mathbf{r})\mathbf{E}(\mathbf{r}, t) = 0 \ , \tag{2.9}$$

$$\nabla \times \mathbf{H}(\mathbf{r}, t) - \frac{\varepsilon(\mathbf{r})}{c}\frac{\partial \mathbf{E}(\mathbf{r}, t)}{\partial t} = 0 \ . \tag{2.10}$$

Both $\mathbf{H}$ and $\mathbf{E}$ are in general complicated functions of time and space. We can separate out the time dependence of the fields since the Maxwell equations are linear. By Fourier analysis, we know that any time dependent function can be rewritten in terms of harmonic modes with appropriate weights. This makes it legitimate to assume that the fields consists of only one frequency component [18]. Then, we simply have

$$\mathbf{E}(\mathbf{r},t) = \mathbf{E}(\mathbf{r})e^{i\omega t} \ , \tag{2.11}$$

$$\mathbf{H}(\mathbf{r},t) = \mathbf{H}(\mathbf{r})e^{i\omega t} \ . \tag{2.12}$$

After this separation of variables thing, we have the curl equations for the field patterns given as

$$\nabla \times \mathbf{E}(\mathbf{r}) + \frac{i\omega}{c}\mathbf{H}(\mathbf{r}) = 0 \ , \tag{2.13}$$

$$\nabla \times \mathbf{H}(\mathbf{r}) - \frac{i\omega}{c}\mathbf{E}(\mathbf{r}) = 0 \ , \tag{2.14}$$

If we decouple these equations with keeping in mind that $\nabla \cdot \varepsilon(\mathbf{r})\mathbf{E}(\mathbf{r}) = 0$ and $\nabla \cdot \mathbf{H}(\mathbf{r}) = 0$, this will yield to

$$\nabla \times \left(\frac{1}{\varepsilon(\mathbf{r})}\nabla \times \mathbf{H}(\mathbf{r})\right) = \left(\frac{\omega}{c}\right)^2 \mathbf{H}(\mathbf{r}) \ , \tag{2.15}$$

where $\mathbf{E}(\mathbf{r})$ could be calculated by

$$\mathbf{E}(\mathbf{r}) = \left(\frac{-ic}{\omega\varepsilon(\mathbf{r})}\right) \nabla \times \mathbf{H}(\mathbf{r}) \ . \tag{2.16}$$

The $\mathbf{H}$ field equation is called the master equation. The reason for choosing this equation is that the differential operator

$$\Theta = \nabla \times \left(\frac{1}{\varepsilon(\mathbf{r})}\nabla \times\right) \ , \tag{2.17}$$

acting on $\mathbf{H}(\mathbf{r})$ from the left is a Hermitian operator, unlike the operator acting on $\mathbf{E}(\mathbf{r})$. We now have an eigenvalue problem for the Hermitian operator Θ. Our eigenvalue problem looks like

$$\Theta\mathbf{H}(\mathbf{r}) = \left(\frac{\omega}{c}\right)^2 \mathbf{H}(\mathbf{r}) \ . \tag{2.18}$$

Here, the eigenvectors $\mathbf{H}(\mathbf{r})$ are the field patterns of the harmonic modes, and the eigenvalues $(\omega/c)^2$ are proportional to the squared frequencies of those modes. Another important point to notice is the linearity of the operator Θ. This means that any linear combination of the solutions is itself a solution. Apparently, the hermiticity and the linearity of the operator of interest will make our lives easier. Let us recall the master equation of the time-independent quantum mechanics, which is

$$H\mathbf{\Psi} = E\mathbf{\Psi};, \tag{2.19}$$

where

$$H = -\frac{\hbar^2}{2m}\nabla^2 + \mathbf{V}(\mathbf{r}) \ . \tag{2.20}$$

One familiar with quantum mechanics will figure out that our problem is the reminiscent of quantum mechanics, and we can safely use the methods developed for solving quantum mechanical problems over the years [19]. One of those many methods is the variational method that is, by the way, a powerful one.

Up to this point, our discussion was very general for any linear electromagnetic problem. Now, it is appropriate to focus on photonic crystals. Photonic crystals are structures possessing a periodically changing dielectric function in space. Namely, the dielectric function satisfies the following relation.

$$\varepsilon(\mathbf{r}) = \varepsilon(\mathbf{r} + \mathbf{a}) \ , \tag{2.21}$$

where $\mathbf{a}$ is the primitive vector of the crystal lattice including all three components. Since $\varepsilon(\mathbf{r})$ is periodic with periodicity $\mathbf{a}$, we can conclude that the operator Θ has translational invariance that means Θ commutes with the discrete translation operator T. The action of T on a space function is that it moves the argument $\mathbf{r}$ of the space function to the new argument $\mathbf{r} + \mathbf{a}$ with keeping the remaining intact. This can mathematically be expressed as

$$Tf(\mathbf{r}) = f(\mathbf{r}+\mathbf{a}) \; . \tag{2.22}$$

The operators Θ and T can be simultaneously diagonalized, because they commute [20]. This is great, because we can guess the eigenfunctions of the translational operator in contrast to the fact that we cannot for Θ. Let our initial guess be the plane wave $e^{i\mathbf{K}\cdot\mathbf{r}}$ where $\mathbf{K}$ is defined by

$$\mathbf{K} = \mathbf{k} + \mathbf{G} \; , \tag{2.23}$$

where

$$-\frac{\pi}{a_i} < \mathbf{k}_i < \frac{\pi}{a_i} \; , \tag{2.24}$$

and

$$\mathbf{G}_i = n\frac{\pi}{a_i} \; . \tag{2.25}$$

Literally, $\mathbf{G}$ is called the $\mathbf{G}$-vector(that goes from the center of the Brillouin zone all the way up to one of the Brillouin zone corners or edges) for any integer n. And $\mathbf{k}$ is the irreducible propagation vector, this will be clear later. In the meantime, we can check the action of T on $e^{i\mathbf{K}\cdot\mathbf{r}}$.

$$Te^{i\mathbf{K}\cdot\mathbf{r}} = e^{i\mathbf{K}\cdot(\mathbf{r}+\mathbf{a})} \; , \tag{2.26}$$

$$Te^{i\mathbf{K}\cdot\mathbf{r}} = e^{i(\mathbf{k}+\mathbf{G})\cdot(\mathbf{r}+\mathbf{a})} \; , \tag{2.27}$$

$$Te^{i\mathbf{K}\cdot\mathbf{r}} = e^{i\mathbf{k}\cdot(\mathbf{r}+\mathbf{a})}e^{i\mathbf{G}\cdot(\mathbf{r}+\mathbf{a})} \; , \tag{2.28}$$

$$Te^{i\mathbf{K}\cdot\mathbf{r}} = e^{i\mathbf{G}\cdot\mathbf{a}}e^{i\mathbf{k}\cdot\mathbf{a}}e^{i(\mathbf{k}+\mathbf{G})\cdot\mathbf{r}} \; , \tag{2.29}$$

$$Te^{i\mathbf{K}\cdot\mathbf{r}} = e^{i\mathbf{k}\cdot\mathbf{a}}e^{i(\mathbf{k}+\mathbf{G})\cdot\mathbf{r}} \; , \tag{2.30}$$

$$Te^{i\mathbf{K}\cdot\mathbf{r}} = e^{i\mathbf{k}\cdot\mathbf{a}}e^{i\mathbf{K}\cdot\mathbf{r}} \; . \tag{2.31}$$

Hence, we can obviously conclude that for any $\mathbf{G}$, $e^{i(\mathbf{k}+\mathbf{G})\cdot\mathbf{r}}$ is an eigenfunction of T with the eigenvalue $e^{i\mathbf{k}\cdot\mathbf{a}}$. One will notice that we have infinite-fold degeneracy, because for any $\mathbf{G}$ the eigenvalue is always $e^{i\mathbf{k}\cdot\mathbf{a}}$. How do we handle this degeneracy? The answer is we simply sum them up over $\mathbf{G}$ with different constants of proportionality. Then our fully operational eigenfunction $\mathbf{H}_k$ that diagonalizes both Θ and T becomes

$$\mathbf{H}_k(\mathbf{r}) = \sum_G \mathbf{h}_G e^{i(\mathbf{k}+\mathbf{G})\cdot\mathbf{r}} \ , \tag{2.32}$$

$$\mathbf{H}_k(\mathbf{r}) = e^{i\mathbf{k}\cdot\mathbf{r}} \sum_G \mathbf{h}_G e^{i\mathbf{G}\cdot\mathbf{r}} \ , \tag{2.33}$$

$$\mathbf{H}_k(\mathbf{r}) = e^{i\mathbf{k}\cdot\mathbf{r}} \mathbf{u}_k(\mathbf{r}) \ , \tag{2.34}$$

where $\mathbf{u}_k(\mathbf{r})$ is obviously a periodic function with periodicity $\mathbf{a}$, or $\mathbf{u}_k(\mathbf{r}) = \mathbf{u}_k(\mathbf{r}+\mathbf{a})$. The form of $\mathbf{H}_k(\mathbf{r})$ is commonly known as a Bloch state in solid state physics and in analytical mechanics as a Floquet mode. After we made use of the the discrete translational symmetry of the photonic crystal, we found out that our eigenstates are just of the Bloch's form.

Now, we may insert $\mathbf{H}_k(\mathbf{r})$ of Bloch's form in the master equation. Then, we have

$$\Theta \sum_G \mathbf{h}_G e^{i(\mathbf{k}+\mathbf{G})\cdot\mathbf{r}} = \left(\frac{\omega}{c}\right)^2 \sum_G \mathbf{h}_G e^{i(\mathbf{k}+\mathbf{G})\cdot\mathbf{r}} \ , \tag{2.35}$$

$$\nabla \times \left(\frac{1}{\varepsilon(\mathbf{r})} \nabla \times \sum_G \mathbf{h}_G e^{i(\mathbf{k}+\mathbf{G})\cdot\mathbf{r}}\right) = \left(\frac{\omega}{c}\right)^2 \sum_G \mathbf{h}_G e^{i(\mathbf{k}+\mathbf{G})\cdot\mathbf{r}} \ , \tag{2.36}$$

$$\nabla \times \left(\frac{(\mathbf{k}+\mathbf{G})}{\varepsilon(\mathbf{r})} \times \sum_G \mathbf{h}_G e^{i(\mathbf{k}+\mathbf{G})\cdot\mathbf{r}}\right) = \left(\frac{\omega}{c}\right)^2 \sum_G \mathbf{h}_G e^{i(\mathbf{k}+\mathbf{G})\cdot\mathbf{r}} \ . \tag{2.37}$$

The other point to mention here is that all $e^{i\mathbf{G}\cdot\mathbf{r}}$ form a complete orthonormal basis since they satisfy

$$\int e^{-i\mathbf{G}'\cdot\mathbf{r}} e^{i\mathbf{G}\cdot\mathbf{r}} d^3\mathbf{r} = \delta_{GG'} \ , \tag{2.38}$$

which means that any function of space can be decomposed into these basis vectors. We can play the same trick for $1/\varepsilon(\mathbf{r})$ as well provided that we have

$$\frac{1}{\varepsilon(\mathbf{r})} = \sum_{G'} \beta_{G'} e^{i\mathbf{G}'\cdot\mathbf{r}} \ , \tag{2.39}$$

$$\beta_{G'} = \frac{1}{V_o} \int \frac{e^{-i\mathbf{G}'\cdot\mathbf{r}}}{\varepsilon(\mathbf{r})} d^3\mathbf{r} \ . \tag{2.40}$$

Using Eq. 2.39 in Eq. 2.37 yields

$$\nabla \times \left(\sum_{G'} \beta_{G'} e^{i\mathbf{G}'\cdot\mathbf{r}} (\mathbf{k}+\mathbf{G}) \times \sum_{G} \mathbf{h}_G e^{i(\mathbf{k}+\mathbf{G})\cdot\mathbf{r}} \right) = \left(\frac{\omega}{c}\right)^2 \sum_{G} \mathbf{h}_G e^{i(\mathbf{k}+\mathbf{G})\cdot\mathbf{r}} \ , \tag{2.41}$$

$$\sum_{G'} \sum_{G} \nabla \times \left(\beta_{G'} e^{i(\mathbf{k}+\mathbf{G}+\mathbf{G}')\cdot\mathbf{r}} (\mathbf{k}+\mathbf{G}) \times \mathbf{h}_G \right) = \left(\frac{\omega}{c}\right)^2 \sum_{G} \mathbf{h}_G e^{i(\mathbf{k}+\mathbf{G})\cdot\mathbf{r}} \ , \tag{2.42}$$

$$\sum_{G'} \sum_{G} \beta_{G'} \nabla \times \left(e^{i(\mathbf{k}+\mathbf{G}+\mathbf{G}')\cdot\mathbf{r}} (\mathbf{k}+\mathbf{G}) \times \mathbf{h}_G \right) = \left(\frac{\omega}{c}\right)^2 \sum_{G} \mathbf{h}_G e^{i(\mathbf{k}+\mathbf{G})\cdot\mathbf{r}} \ , \tag{2.43}$$

$$\sum_{G'} \sum_{G} \beta_{G'} (\mathbf{k}+\mathbf{G}+\mathbf{G}') \times \{(\mathbf{k}+\mathbf{G}) \times \mathbf{h}_G\} \, e^{i(\mathbf{k}+\mathbf{G}+\mathbf{G}')\cdot\mathbf{r}} = \left(\frac{\omega}{c}\right)^2 \sum_{G} \mathbf{h}_G e^{i(\mathbf{k}+\mathbf{G})\cdot\mathbf{r}} \ . \tag{2.44}$$

After we made the change $\mathbf{G}' \longrightarrow \mathbf{G}' - \mathbf{G}$, we have

$$\sum_{G'} \sum_{G} \beta_{G'-G} (\mathbf{k}+\mathbf{G}') \times \{(\mathbf{k}+\mathbf{G}) \times \mathbf{h}_G\} \, e^{i(\mathbf{k}+\mathbf{G}')\cdot\mathbf{r}} = \left(\frac{\omega}{c}\right)^2 \sum_{G'} \mathbf{h}_{G'} e^{i(\mathbf{k}+\mathbf{G}')\cdot\mathbf{r}} \ . \tag{2.45}$$

We know that the coefficients of the plane waves must be the same for the sum on the left-hand side and the right-hand side, thus

$$\sum_{G} \beta_{G'-G} (\mathbf{k}+\mathbf{G}') \times \{(\mathbf{k}+\mathbf{G}) \times \mathbf{h}_G\} = \left(\frac{\omega}{c}\right)^2 \mathbf{h}_{G'} \ . \tag{2.46}$$

Using the vector identities, our equation transforms to

$$\sum_G \beta_{G'-G}\{(\mathbf{k}+\mathbf{G}')\cdot(\mathbf{k}+\mathbf{G})\}\mathbf{h}_G - \{(\mathbf{k}+\mathbf{G}')\cdot\mathbf{h}_G\}(\mathbf{k}+\mathbf{G}) = \left(\frac{\omega}{c}\right)^2 \mathbf{h}_{G'} \ . \quad (2.47)$$

Since $\mathbf{h}_{G'}$ should be perpendicular to $\mathbf{k}+\mathbf{G}'$ in accord to the transversality condition, our eigenvalue problem becomes

$$\sum_G \beta_{G'-G}\{(\mathbf{k}+\mathbf{G}')\cdot(\mathbf{k}+\mathbf{G})\}\mathbf{h}_G = \left(\frac{\omega}{c}\right)^2 \mathbf{h}_{G'} \ . \quad (2.48)$$

By solving this equation numerically, we can obtain the dispersion relation of the eigenmodes, or the photonic band structure in addition to the eigenmodes themselves [21, 22]. This numerical method, which is based on the Fourier expansion of the electromagnetic field and the dielectric function is called the photonic plane wave expansion method. In a real numerical calculation of the photonic band structure, the summation in the above matrix equation is calculated up to a sufficiently large number N of $\mathbf{G}$, and an eigenvalue problem for each $\mathbf{k}$ is solved. This is equivalent to diagonalization of the matrix defined by the left-hand side of the above equation. The dimension of the matrix to be diagonalized is $2N$, since $\mathbf{h}_{G'}$ should be perpendicular to $\mathbf{k}+\mathbf{G}'$ in accord to the transversality condition. The CPU time for the photonic band calculation by means of the plane wave expansion method is proportional to N^3.

In this thesis we focus on two-dimensional photonic crystals, so let's solve the matrix eigenvalue equation that we have derived from a differential version of the eigenvalue problem. The first thing to do here is to determine the form of the components $\beta_{G'-G}$ of the inverse dielectric function. Now, we assume that we have a square array, having a period of $\mathbf{a}$, of circular dielectric rods of radius r_r with dielectric index ε_r in air(Fig. 2.1). Because our structure is uniform in the z direction, we restrict our discussion to $\mathbf{G}$ vectors in the plane of the photonic crystal. In mathematical terms the periodic dielectric function can be written as

$$\frac{1}{\varepsilon(\mathbf{r})} = 1 + \left(\frac{1}{\varepsilon_r} - 1\right) S(\mathbf{r}) \ , \quad (2.49)$$

where $S(\mathbf{r})$ is 1 for $|r| \leq r_r$, and is 0 otherwise.

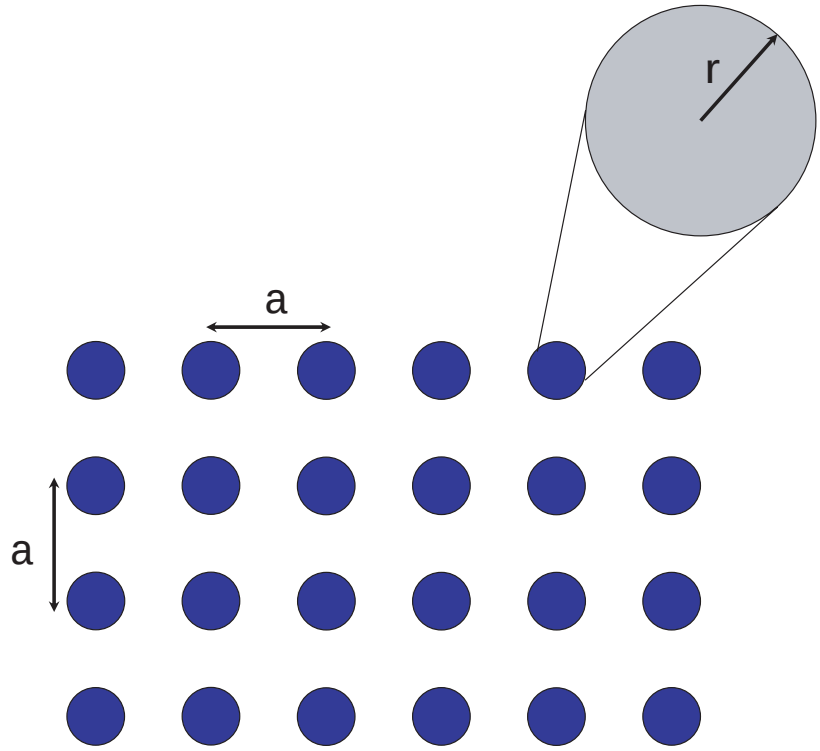

Figure 2.1: Our square photonic lattice of dielectric rods in air.

Substituting Eq. 2.49 into Eq. 2.40,

$$\beta_G = \delta_{G0} + \frac{1}{V_o}\left(\frac{1}{\varepsilon_r} - 1\right)\int S(\mathbf{r})e^{-i\mathbf{G}\cdot\mathbf{r}}d^3\mathbf{r}\ . \tag{2.50}$$

We will use cylindrical polar coordinates in order to calculate the integral in the equation above. Hence, β_G is equal to

$$\delta_{G0} + \frac{1}{V_o}\left(\frac{1}{\varepsilon_r} - 1\right)\int_0^{r_r} r dr \int_0^{2\pi} d\varphi e^{-iGr\cos\varphi}\ , \tag{2.51}$$

$$\delta_{G0} + \frac{1}{V_o}\left(\frac{1}{\varepsilon_r} - 1\right)\int_0^{r_r} r dr \int_0^{2\pi} d\varphi \sum_l J_l(Gr)e^{il(\varphi-\frac{\pi}{2})}\ , \tag{2.52}$$

$$\delta_{G0} + \frac{2\pi}{V_o}\left(\frac{1}{\varepsilon_r} - 1\right)\int_0^{r_r} r J_0(Gr)dr\ , \tag{2.53}$$

$$= \delta_{G0} + \frac{2\pi r_r}{GV_o}\left(\frac{1}{\varepsilon_r} - 1\right)J_1(Gr_r)dr\ . \tag{2.54}$$

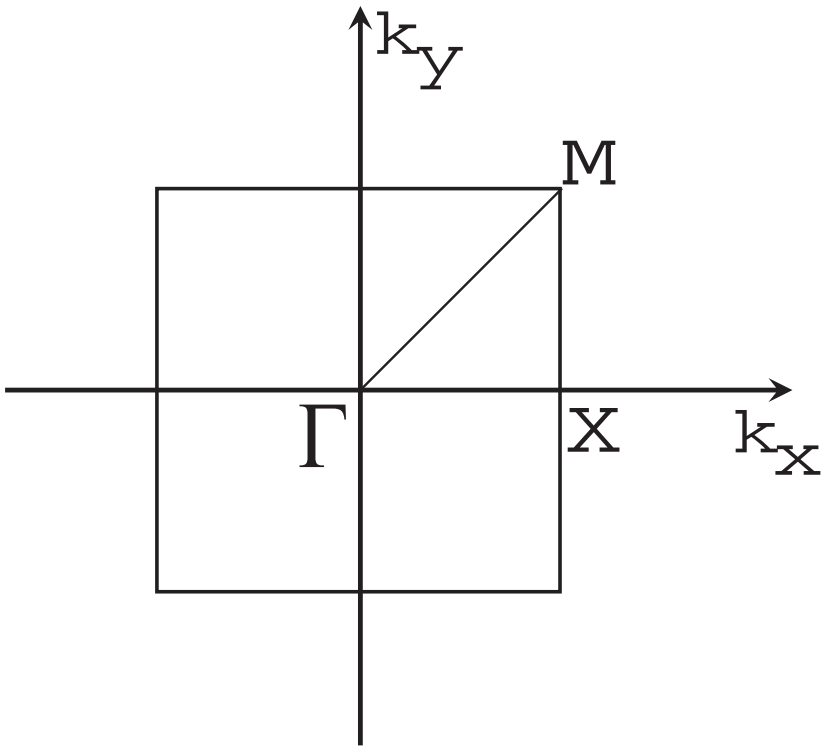

Figure 2.2: The first Brillouin zone for our square photonic crystal. The triangle represents the irreducible Brillouin zone. This is determined by making use of the symmetries of the photonic crystal, namely the rotational, reflection, and time-reversal symmetries. The most symmetric points of the Fourier (momentum, or indirect) space are also shown in the figure.

After having determined β_G we will construct the matrix to diagonalize for both TM and TE polarized electromagnetic waves [23]. We can first consider the TE polarization, **H**-field is parallel to the dielectric rods. The matrix to be diagonalized for this polarization is

$$\begin{bmatrix} \beta_{11}\mathbf{k}\cdot\mathbf{k} & \beta_{12}\mathbf{k}\cdot(\mathbf{k}+\mathbf{G_1}) & \cdots & \beta_{1N}\mathbf{k}\cdot(\mathbf{k}+\mathbf{G_{N-1}}) \\ \beta_{21}(\mathbf{k}+\mathbf{G_1})\cdot\mathbf{k} & \beta_{22}(\mathbf{k}+\mathbf{G_1})^2 & \dots & \beta_{2N}(\mathbf{k}+\mathbf{G_1})\cdot(\mathbf{k}+\mathbf{G_{N-1}}) \\ \vdots & \vdots & \vdots & \vdots \\ \vdots & \vdots & \vdots & \vdots \\ \beta_{N1}(\mathbf{k}+\mathbf{G_{N-1}})\cdot\mathbf{k} & \dots & \dots & \beta_{NN}((\mathbf{k}+\mathbf{G_{N-1}})^2 \end{bmatrix}. \tag{2.55}$$

As we have already mentioned, we will diagonalize this matrix for each $\mathbf{k}$ in the momentum space. As a result of this process, we will have a series of eigenvalues for each $\mathbf{k}$, and when the calculation is completed for all vectors the eigenvalues will group to form a photonic band.

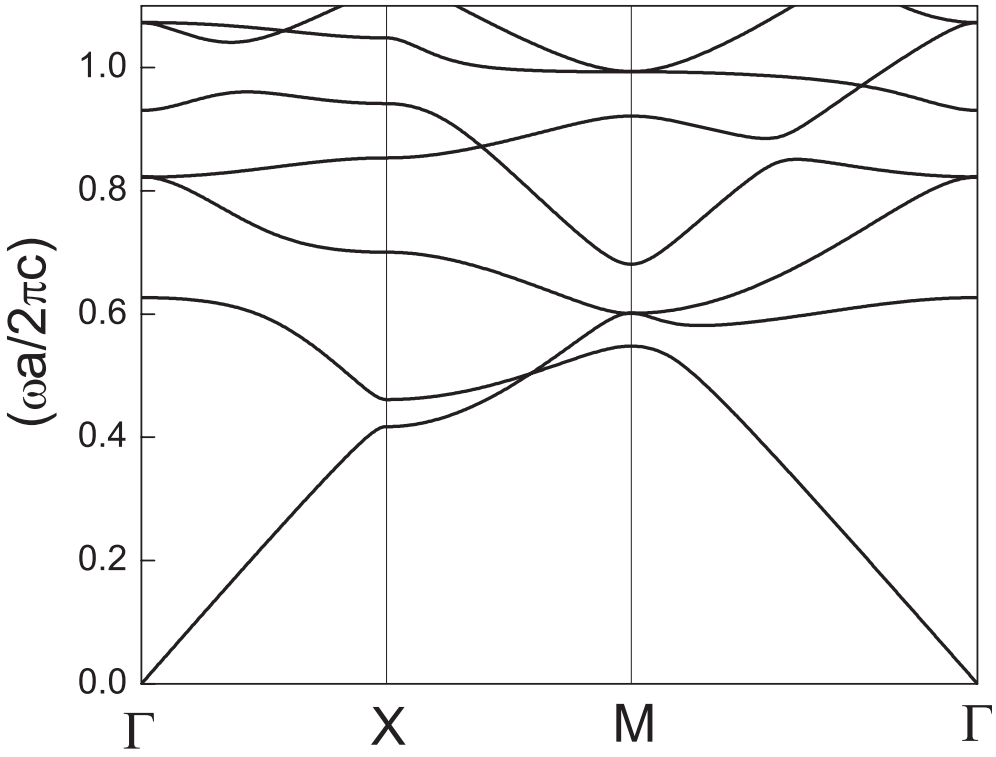

Figure 2.3: The TE polarized band structure of our square photonic crystal. The first seven bands are shown here. As can be seen from this figure, our structure does not exhibit a photonic band gap for this polarization.

To minimize the calculation time, we can for sure make use of the symmetries of our structures. Our structure apparently exhibits translational symmetry so

we will restrict ourselves to the first Brillouin zone (the square seen in Fig. 2.2). We can go further, we also have the time reversal symmetry, which implies propagating in the direction of k_x or $-k_x$ are physically identical, and this holds for k_y and $-k_y$ as well. Now in turn we can focus on the upper left quadrant of the first Brillouin zone. And there is one more to consider that is the rotational symmetry since our structure is invariant under rotations of 45°. Consequently, we can characterize our photonic band structure just by analyzing for **k**-vectors lying in or on the triangle shown in Fig. 2.2. Subsequently, by setting $r = 0.2a$, and $\varepsilon_r = 9$ we have calculated the TE polarized band structure of our square photonic crystal as shown in Fig. 2.3. Namely, we have determined the first 7 eigenvalues of each **k** vector along these special symmetry directions. And obviously these eigenvalues automatically corresponds to a photonic dispersion relation $\omega(\mathbf{k})$ (all these seven bands determine the dispersion for their frequency range span) when plotted all together. No photonic band gap is observed for this polarization.

Meanwhile, we can calculate the band structure for TM polarized electromagnetic waves, the **E**-field parallel to the dielectric rods. For this case, our eigenvalue problem becomes

$$\sum_G \beta_{G'-G}\{(\mathbf{k}+\mathbf{G}')\cdot(\mathbf{k}+\mathbf{G})\}(\mathbf{h}_{G_x}+\mathbf{h}_{G_y}) = \left(\frac{\omega}{c}\right)^2 (\mathbf{h}_{G_x}+\mathbf{h}_{G_y})\ . \tag{2.56}$$

By transforming this equation into a matrix equation, we have

$$\begin{bmatrix} \beta_{11}\mathbf{k}\cdot\mathbf{k} & \beta_{11}\mathbf{k}\cdot\mathbf{k} & \cdots & \beta_{1N}\mathbf{k}\cdot(\mathbf{k}+\mathbf{G_{N-1}}) \\ \beta_{21}(\mathbf{k}+\mathbf{G_1})\cdot\mathbf{k} & \beta_{21}(\mathbf{k}+\mathbf{G_1})\cdot\mathbf{k} & \dots & \beta_{2N}(\mathbf{k}+\mathbf{G_1})\cdot(\mathbf{k}+\mathbf{G_{N-1}}) \\ \vdots & \vdots & \vdots & \vdots \\ \vdots & \vdots & \vdots & \vdots \\ \beta_{N1}(\mathbf{k}+\mathbf{G_{N-1}})\cdot\mathbf{k} & \beta_{N1}(\mathbf{k}+\mathbf{G_{N-1}})\cdot\mathbf{k} & \dots & \beta_{NN}(\mathbf{k}+\mathbf{G_{N-1}})^2 \end{bmatrix}, \tag{2.57}$$

to diagonalize. We should note that this time the dimension of our matrix is $2N$ in contrast to the matrix having a dimension of N for the other polarization. Diagonalizing this matrix in a similar way for the **k** vectors along the symmetry

direction yields to the band structure displayed in Fig. 2.4. As seen in Fig. 2.4, in this configuration the bands form in such a fashion that we have a well-defined photonic band gap lying in between the first (valence) and the second (conduction) band of the photonic crystal. This gap region is shaded for convenience. There are no allowed photonic modes within this forbidden frequency range. So, electromagnetic waves having frequencies lying within this range can not couple to the propagating photonic modes of the photonic crystal, nor be transmitted. Since at the very beginning we introduces lossless materials, all of the incident power is expected to be reflected back from our photonic crystal.

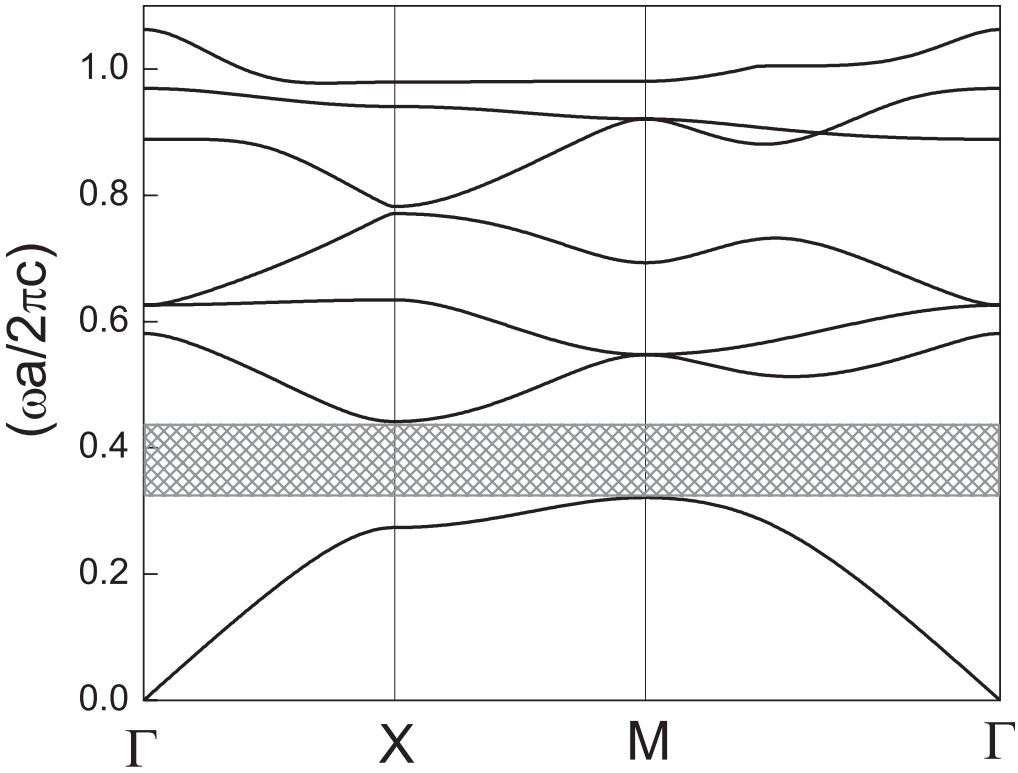

Figure 2.4: The TM polarized band structure of our square photonic crystal. The first seven bands are shown here. As can be seen from this figure, our structure exhibits a photonic band gap for this polarization.

If we desire to calculate the field patterns of the photonic modes we can simply solve our eigenvalue problem for the eigenvectors. After determining the components of the eigenvectors we can construct the eigenfield pattern in space

just inserting the coefficients in

$$\mathbf{H}_{nk}(\mathbf{r}) = \sum_{G} \sum_{j=1}^{2} \mathbf{h}_{jG}^{(n)} e^{i(\mathbf{k}+\mathbf{G})\cdot\mathbf{r}} \hat{\mathbf{e}}_j \ . \tag{2.58}$$

Here, n is the photonic band index, and j determines the vector components of $\mathbf{H}_{nk}(\mathbf{r})$. We can calculate $\mathbf{E}_{nk}(\mathbf{r})$ as well through the relation

$$\mathbf{E}_{nk}(\mathbf{r}) = \left(\frac{-ic}{\omega_n(\mathbf{k})\varepsilon(\mathbf{r})} \right) \nabla \times \mathbf{H}_{nk}(\mathbf{r}) \ , \tag{2.59}$$

$$\mathbf{E}_{nk}(\mathbf{r}) = \left(\frac{-ic}{\omega_n(\mathbf{k})\varepsilon(\mathbf{r})} \right) \nabla \times \sum_{G} \sum_{j=1}^{2} \mathbf{h}_{jG}^{(n)} e^{i(\mathbf{k}+\mathbf{G})\cdot\mathbf{r}} \hat{\mathbf{e}}_j \ . \tag{2.60}$$

So, we can conclude that

$$\mathbf{E}_{nk}(\mathbf{r}) = \left(\frac{c}{\omega_n(\mathbf{k})\varepsilon(\mathbf{r})} \right) \sum_{G} \sum_{j=1}^{2} \mathbf{h}_{jG}^{(n)} e^{i(\mathbf{k}+\mathbf{G})\cdot\mathbf{r}} [(\mathbf{k}+\mathbf{G}) \times \hat{\mathbf{e}}_j] \ . \tag{2.61}$$

Up to this point we have successfully developed a comprehensive method to determine the dispersion relation of the radiation modes in photonic crystal as well as the photonic eigenmodes themselves. In addition to these, we can also introduce several new parameters to characterize the eigenmodes of the photonic crystal. The waves are characterized by three velocities, namely phase, group, and energy velocities. These are all equal in uniform materials with dielectric constants, which are real and independent of frequency. The phase velocity is defined as the the velocity of the propagation of a phase front. This velocity has a definite meaning, for instance the phase front (equal phase surface) can be defined for plane waves unambiguously. Contrary to that, the equal phase surface can not be defined conveniently, since as seen in Eq. 2.61 the eigenmode of a photonic crystal is a superposition of many plane waves. The group and the energy velocities can be proven to be equal in a photonic crystal. So, we can just consider group velocity rather than both. The group velocity that is defined as the velocity of the propagation of a wave packet can be calculated by

$$\mathbf{v_g} = \nabla_k \omega_n(\mathbf{k}) \ . \tag{2.62}$$

Since we are working numerically, we can represent this for our two dimensional photonic crystal as

$$\mathbf{v_g} = \left(\lim_{\Delta k_x \to 0} \frac{\omega_n(k_x + \Delta k_x, k_y) - \omega_n(k_x, k_y)}{\Delta k_x} \right) \hat{x} + \left(\lim_{\Delta k_y \to 0} \frac{\omega_n(k_x, k_y + \Delta k_y) - \omega_n(k_x, k_y)}{\Delta k_y} \right) \hat{y} \, . \tag{2.63}$$

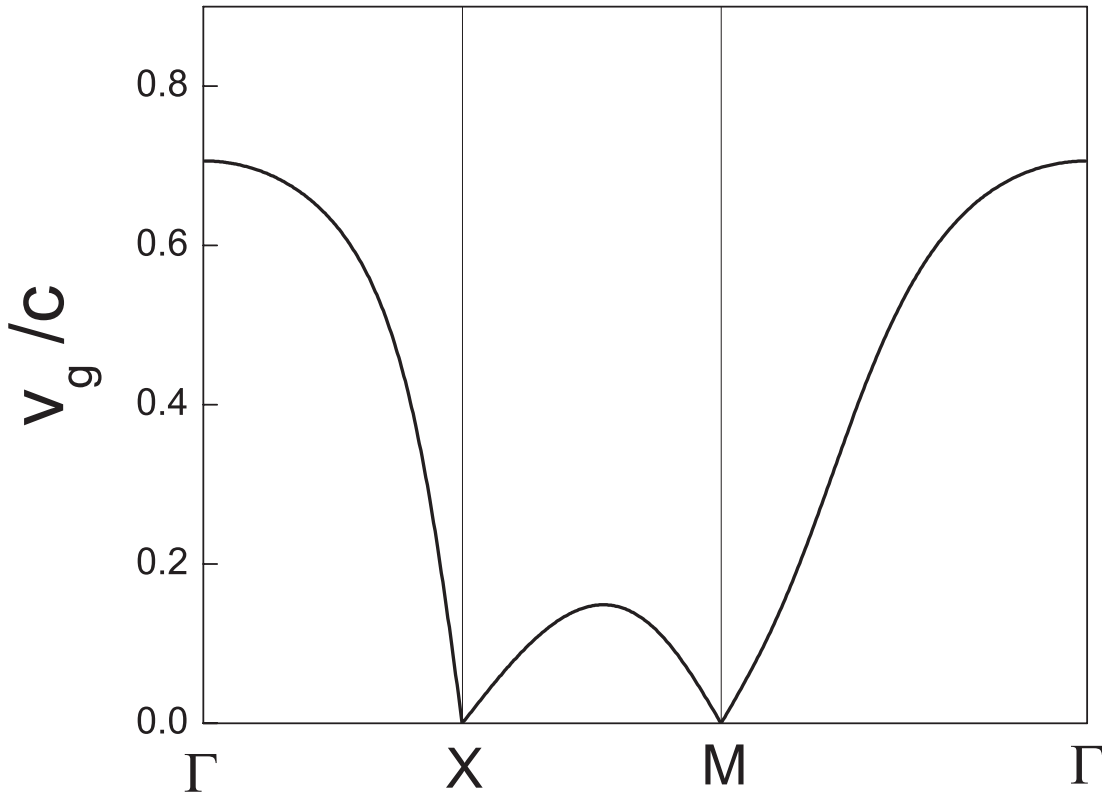

Figure 2.5: The group velocity distribution of the valence band calculated by Hellmann-Feynmann method. The group velocity drastically goes to zero at the photonic band edges.

This numerical differentiation needs a limiting procedure for which we have to know a series of eigenfrequencies as a function of the wave vector (we need to diagonalize our matrix for many wave vectors for accuracy). There is an alternative, named the Hellmann-Feynman theorem, to this differentiation procedure. To implement this theorem we must have a Hermitian operator and the orthonormal basis composed of the eigenmodes of that operator. We already have this preliminary conditions, and using the hermiticity of our operator we have derived Eq. 2.48 so let us start with multiplying both sides of that equation by $\mathbf{h}_{G'}$. This yields

$$\sum_G \beta_{G'-G}\{(\mathbf{k}+\mathbf{G}')\cdot(\mathbf{k}+\mathbf{G})\}\mathbf{h}_G\cdot\mathbf{h}_{G'} = \left(\frac{\omega}{c}\right)^2 \mathbf{h}_{G'}\cdot\mathbf{h}_{G'} \ . \tag{2.64}$$

Now we can sum both sides over G'.

$$\sum_{G'}\sum_G \beta_{G'-G}\{(\mathbf{k}+\mathbf{G}')\cdot(\mathbf{k}+\mathbf{G})\}\mathbf{h}_G\cdot\mathbf{h}_{G'} = \left(\frac{\omega}{c}\right)^2 \sum_{G'}\mathbf{h}_{G'}\cdot\mathbf{h}_{G'} \ . \tag{2.65}$$

The sum on the left-hand side of the equation is equal to unity because the eigenvectors are orthonormal. Then we have

$$\sum_{G'}\sum_G \beta_{G'-G}\{(\mathbf{k}+\mathbf{G}')\cdot(\mathbf{k}+\mathbf{G})\}\mathbf{h}_G\cdot\mathbf{h}_{G'} = \left(\frac{\omega}{c}\right)^2 \sum_{G'}\mathbf{h}_{G'}\cdot\mathbf{h}_{G'} \ . \tag{2.66}$$

By taking the gradient, our identity becomes

$$\nabla_k \sum_{G'}\sum_G M_{GG'}\mathbf{h}_G\cdot\mathbf{h}_{G'} = \nabla_k\left(\frac{\omega}{c}\right)^2 \ , \tag{2.67}$$

where

$$M_{GG'} = \beta_{G'-G}(\mathbf{k}+\mathbf{G}')\cdot(\mathbf{k}+\mathbf{G}) \ , \tag{2.68}$$

$$M_{GG'} = \beta_{G'-G}[(k_x+G_x)(k_x+G'_x)+(k_y+G_y)(k_y+G'_y)] \ . \tag{2.69}$$

Then we have

$$\frac{2\omega}{c^2}\nabla_k\omega = \sum_{G'}\sum_G \mathbf{h}_G\cdot\mathbf{h}_{G'}\nabla_k M_{GG'} \ , \tag{2.70}$$

$$\nabla_k\omega = \frac{c^2}{2\omega}\sum_{G'}\sum_G \mathbf{h}_G\cdot\mathbf{h}_{G'}\nabla_k M_{GG'} \ , \tag{2.71}$$

$$\mathbf{v_g} = \frac{c^2}{2\omega}\sum_{G'}\sum_G \mathbf{h}_G\cdot\mathbf{h}_{G'}\nabla_k M_{GG'} \ . \tag{2.72}$$

The gradient on the left-hand side of the above equation is

$$\nabla_k M_{GG'} = \beta_{G'-G}\nabla_k[(k_x+G_x)(k_x+G'_x)+(k_y+G_y)(k_y+G'_y)] \ , \tag{2.73}$$

$$\nabla_k M_{GG'} = \beta_{G'-G}[(2k_x + G_x + G'_x)\hat{x} + (2k_y + G_y + G'_y)\hat{y}] \ , \tag{2.74}$$

Using this in Eq. 2.72 yields

$$\mathbf{v_g} = \frac{c^2}{2\omega} \sum_{G'} \sum_{G} \mathbf{h}_G \cdot \mathbf{h}_{G'} \beta_{G'-G}[(2k_x + G_x + G'_x)\hat{x} + (2k_y + G_y + G'_y)\hat{y}] \ . \tag{2.75}$$

Therefore, the group velocity can be evaluated once the eigenvector $\mathbf{h_G}$ and the eigenvalue ω are obtained by the band calculation based on the photonic plane-wave expansion method. We have calculated the group velocities of the first TM polarized band of our structure in different direction on the reduce Brillouin zone. The magnitudes of the group velocity versus the $\mathbf{k}$ vectors are plotted in Fig. 2.5. As one will notice the group velocity drastically goes to zero at the reduced Brillouin zone corners, these correspond to the photonic band edges for the first band. So for a finite size photonic crystal we expect extremely low group velocities at the photonic band edges. Low group velocity concept are of general interest in the area of the nonlinear processes, lasing action, and directional radiation sources since all are enhanced as the group velocities of interest get smaller.

The transmission spectra of photonic crystals reflect their band structure directly. They are often used for the experimental characterization of real samples. In the remaining, we will briefly discuss the Finite Difference Time Domain method for the calculation of the transmission, reflection, and as well as the band structure of photonic crystals. As one note that in the photonic plane wave expansion method we have focused on infinitely large structures, which are periodic. In the finite difference time domain method, we can characterize any finite size electromagnetic structure including photonic crystals of linear, nonlinear, or dispersive, namely metallic type. The finite difference time domain method, introduced by Yee, is full-wave, dynamic, and powerful solution tool for solving the Maxwell's equations. This method to electromagnetic waves is more than what the Density Functional Theory is to electrons, since we can calculate the time evolution of the electromagnetic waves in any medium. The fundamental ingredient of the algorithm involves direct discretization of the time dependent Maxwell's equation by writing the spatial and time derivatives in a central finite

difference form. This approximation is second-order accurate in both space and time, and it requires the electric and magnetic fields to be offset from one another in space. Furthermore, this two-step, leap-frogging algorithm requires the electric and magnetic fields to be updated at staggered half-time steps. The update algorithm is explicit, so new values of electromagnetic field components depend only on these values at the previous time and half-time steps. The algorithm provides a complete full-wave electromagnetic solution simply in one computational run.

Chapter 3

Negative refraction

Refraction is perhaps one of the most basic of electromagnetic phenomena, whereby when a beam of radiation is incident on an interface between two media at an arbitrary angle, and the direction of propagation of the transmitted beam is altered by an amount related to the indices of refraction of the two media. We know that we can define the plane waves with the complex amplitudes $e^{i\mathbf{k_i}\cdot\mathbf{r}}$ and $e^{i\mathbf{k_r}\cdot\mathbf{r}}$ in the the first and the second medium, respectively. By requiring that the phase of the incident and transmitted beams be the same everywhere at the interface, we can arrive at the Snell's law, which provides the quantitative relation between the incident and refractive angles θ_i and θ_r (both are measured from the interface normal) and the indices of refraction of the media n_i and n_r(Fig. 3.1). Mathematically, the conservation of the phase along the boundary is given as

$$\mathbf{k_i} \cdot \mathbf{r}_{||} = \mathbf{k_r} \cdot \mathbf{r}_{||} \ , \tag{3.1}$$

$$k_i r_{||} \cos(\frac{\pi}{2} - \theta_i) = k_r r_{||} \cos(\frac{\pi}{2} - \theta_i) \ . \tag{3.2}$$

By using the basic relation between the energy and the momentum of a plane wave inside a medium as $k = n\omega/c$, we have

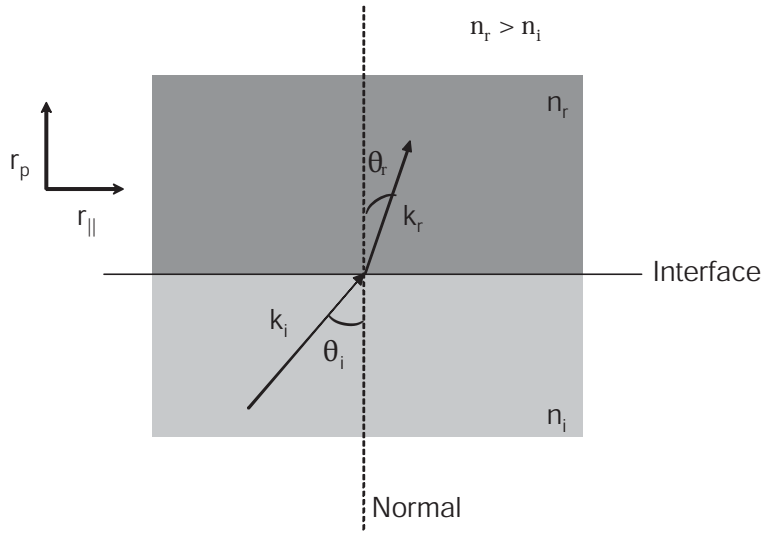

Figure 3.1: Schematics of refraction of electromagnetic waves transmitting through an interface between two dielectric media.

$$n_i \frac{\omega_i}{c} \sin\theta_i = n_r \frac{\omega_r}{c} \sin\theta_r \ . \tag{3.3}$$

And since the energy is conserved, namely $\omega_i = \omega_r$, we end up with the famous Snell's law given as

$$n_i \sin\theta_i = n_r \sin\theta_r \ . \tag{3.4}$$

Thus, a refracted ray is bent toward the normal upon entering a naturally occurring medium from air, as most media have $n_r > 1$, but never emerges on the same side of the normal as the incident ray. Refraction forms the basis of lenses and imaging, as any finite section of material with an index differing from that of its environment will alter the direction of incoming rays that are not normal to the interface. Lenses can be designed to focus and steer radiation for a variety of applications and are of use over a large range of wavelengths extending from optical to radio.

The best way to analyze the refractive properties of any medium is using the Equal Frequency Contours (EFC) of the medium. To determine the EFC of a medium, we first need to determine the dispersion relation $\omega(\mathbf{k}) = \omega(k_x, k_y)$ of that medium. For a linear medium having an index of refraction n we have the dispersion relation as

$$\omega(\mathbf{k}) = \omega(k_x, k_y) = \sqrt{k_x^2 + k_y^2}c/n \ , \tag{3.5}$$

or

$$k_x^2 + k_y^2 = \left(\frac{n\omega}{c}\right)^2 \ . \tag{3.6}$$

This equation defines a circle with radius $n\omega/c$ in the momentum space. And as the frequency changes as a parameter we can represent our dispersion relation as a cone as seen in Fig. 3.2.

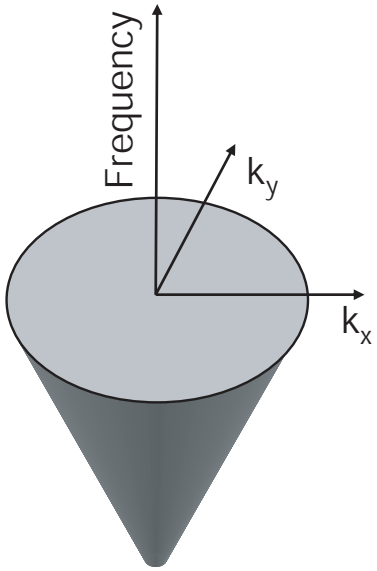

Figure 3.2: Two dimensional dispersion relation of uniform frequency independent linear medium in the **k**-space.

Now, we will assume that a plane wave of frequency ω_o is incident from air to a medium of refractive index n. First we will draw the EFC of air, which is simply a circle with radius $k_{air} = \omega_o/c$ in the momentum space as shown in Fig. 3.3, and let the wave that is incident from air to the medium makes an angle of θ_1 with the interface normal. The group velocity of the wave in air, which is the gradient of the EFC at the point where the wave vector touches the EFC is also shown. Since we simply have a circular EFC, the wave vector and the group velocity are both oriented in the same direction. We should also keep in mind that we are employing the ray picture of light in this discussion. We also know that the component of the wave vector that is parallel to the interface must be conserved at the boundary. This will in turn determine the wave that will be excited in the

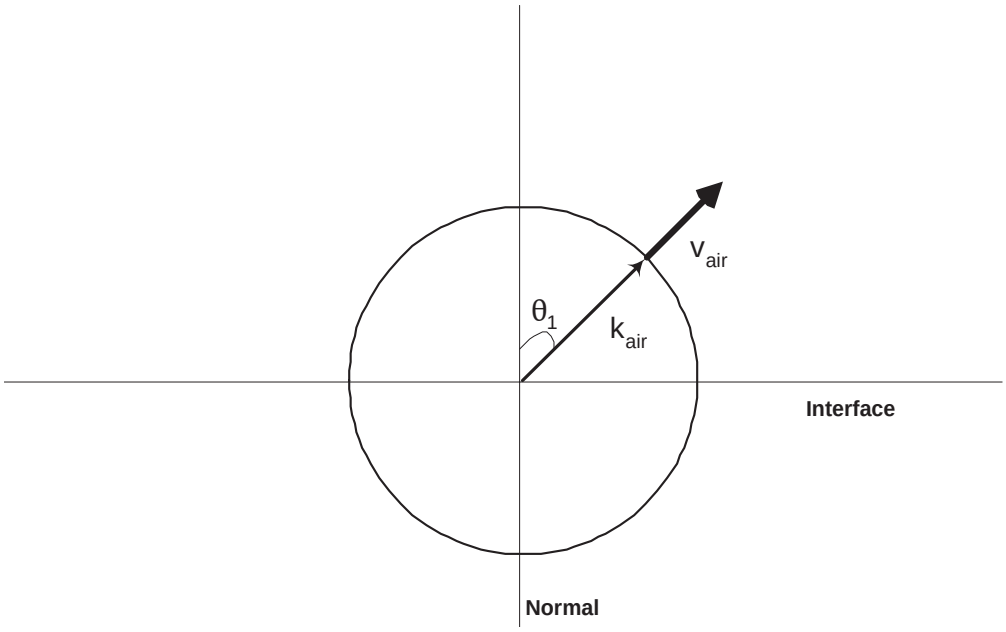

Figure 3.3: The equal frequency of contour of air for frequency ω_o. The wave vector and the group velocity for our incident wave are also drawn.

second medium. The dashed line in Fig. 3.4 represents the parallel wave vector conservation. After this line, we draw the the EFC of the medium having an index of refraction of n. This contour is a circle of radius $k_m = n\omega_o/c$ in the momentum space as seen in Fig. 3.4. The intersection of the dashed line with the EFC of the medium determines the direction of the wave vector in the medium. Since the EFS is circular for this medium, the group velocity that is calculated by taking the gradient of the EFC is parallel to the the wave vector in the medium. In the meantime one can notice that the conservation of the surface parallel wave vector gives us nothing but the Snell's law. So, our claim that we can characterize refraction of electromagnetic waves by the use of the equal frequency contours turns out to be true. The analysis becomes more complicated for a grating that has a periodically repeating equal frequency contour in the momentum space. For this kind of grating medium the Snell's law no more determines the propagation direction, because we will have diffracted or Bragg waves as well.

After having developed the basics of refraction we can consider the special cases of this phenomenon. One of these special cases is the negative refraction. Although all of the known naturally occurring materials exhibit positive indices

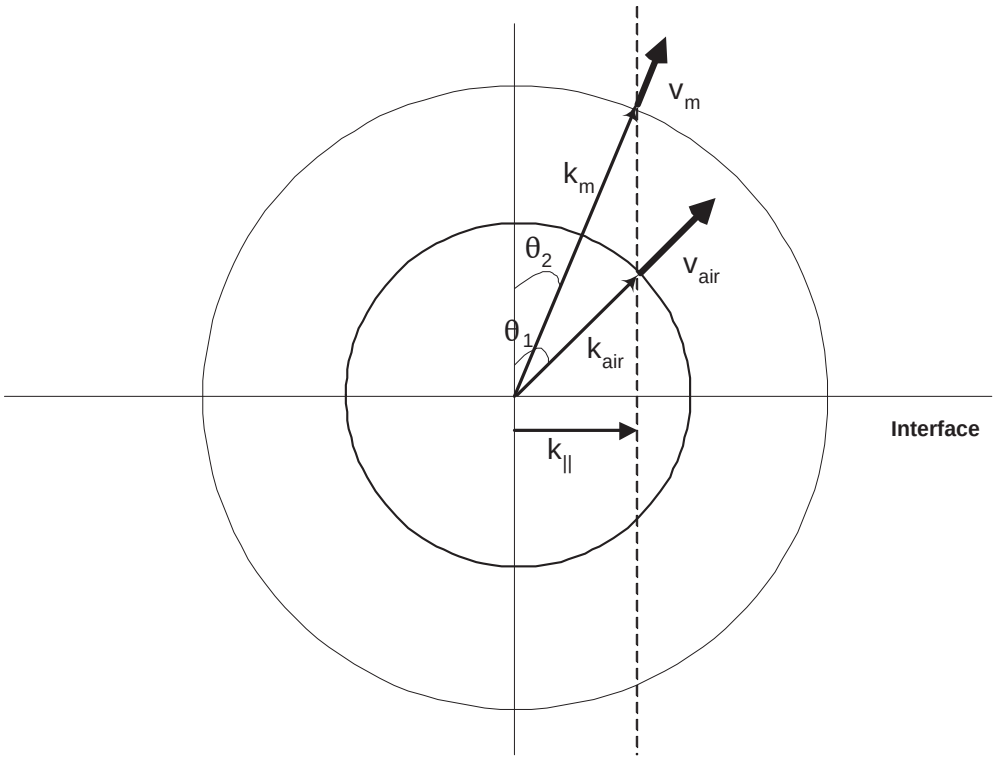

Figure 3.4: The equal frequency of contours of air and the dielectric medium having refractive index n for frequency ω_o. The wave vector and the group velocity for our incident wave are also drawn.

of refraction, the possibility of materials with negative refractive index has been explored theoretically by Victor Veselago [24]. In this seminal work, he concluded that such materials did not violate any fundamental physical laws. These materials were termed left-handed materials (LHMs), and it was further shown that some of the most fundamental electromagnetic properties of an LHM would be opposite to that of ordinary right-handed materials (RHM), resulting in unusual and nonintuitive optics. A beam incident on an LHM from an RHM, for example, refracts to the same side of the normal as the incident ray. Furthermore, it was predicted that the rays from a point source impinging on a flat, parallel slab of LHM would be refocused to a point on the opposite side of the material. Recently, analysis of this situation produced the observation that such a planar slab, with a suitable index, can be used to achieve focusing with subwavelength resolution, beating the normal diffraction limit associated with positive refractive index optics [25].

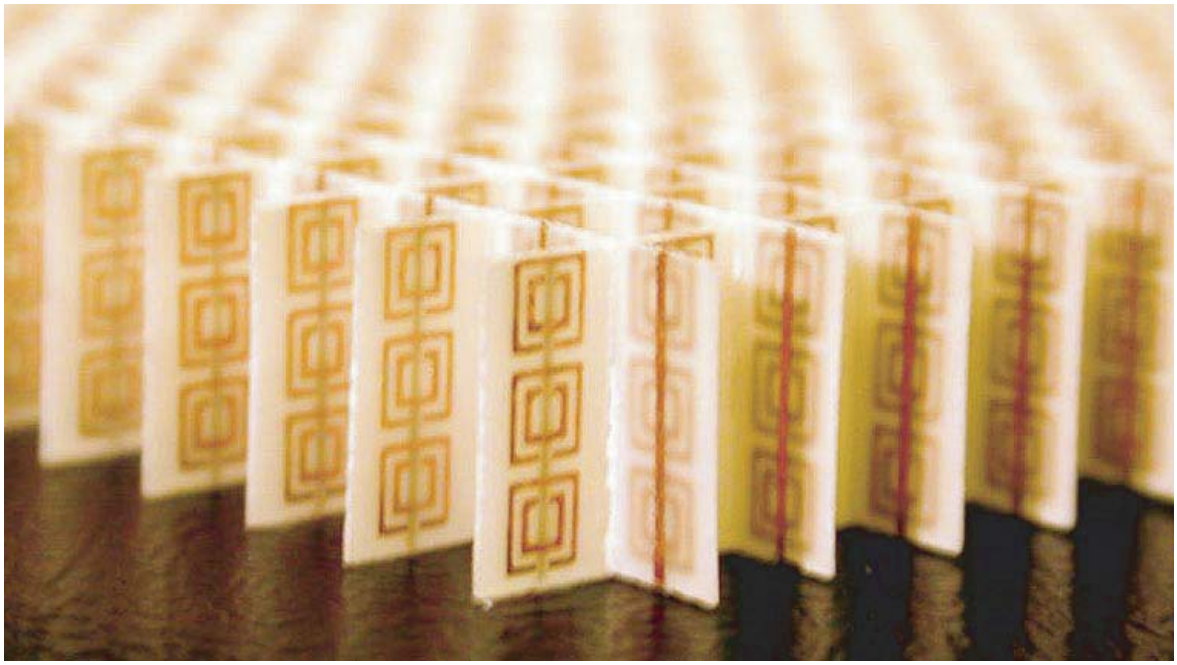

Figure 3.5: Photograph of the left-handed metamaterial (LHM) sample used by UCSD team. The LHM sample consists of square copper split ring resonators and copper wire strips on fiber glass circuit board material. The rings and wires are on opposite sides of the boards, and the boards have been cut and assembled into an interlocking lattice.

The fabrication and measurement of structured metamaterials having a range of frequencies over which the refractive index was predicted to be negative for one direction of propagation were reported recently by Smith *et al* [26]. An extension of this structure to two dimensions was subsequently introduced and predicted to exhibit an isotropic, negative index in two dimensions [27]. These structures use split ring resonators to produce negative magnetic permeability over a particular frequency region and wire elements to produce negative electric permittivity in an overlapping frequency region. The negative permittivity to visible light of some metals, such as silver, had been established well before Veselagos original studies. Pendry, who was developing devices to control the microwaves used in radar systems, was interested in developing materials with negative permeability [28]. Both permittivity and permeability depend on the collective response of the electrons within a material to the applied electric and magnetic fields. To control this response, Pendry proposed an array of closely spaced, thin, conducting elements,

such as metal hoops, which as a whole behaved as a kind of composite material. In 1999, Pendry described how he adjusted the array properties, such as the spacing between the elements, to create an array with negative permeability.

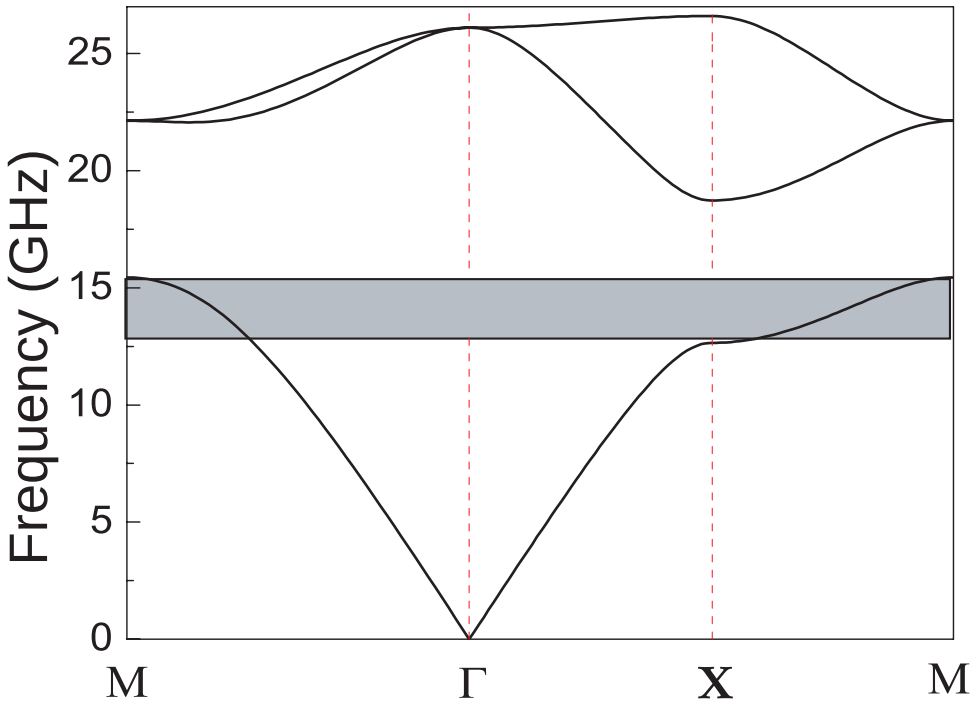

Figure 3.6: TM polarized band structure of our photonic crystal along the symmetry directions. The frequency region within which negative refraction is expected to occur is also indicated by the gray area.

When the permittivity, ε, and permeability, μ, of a material are simultaneously negative, one must choose the negative root of the index of refraction given by $n = \pm\sqrt{\varepsilon\mu}$ (1, 2, 7). Following up on Pendry's work and the idea above, Smith *et al.* reported a meta-material with a negative refractive index, which consists of interlocking units of thin fiberglass sheets imprinted with copper rings and wires. They tested the refractive properties of this meta-material by measuring an incident microwave beam and found that Veselagos original calculation was correct: the microwaves were bent in the opposite direction from normal [29]. This was the first evidence that the negative refraction is achievable in artificially engineered materials.

We can explore the possibility of negative refraction in photonic crystals as

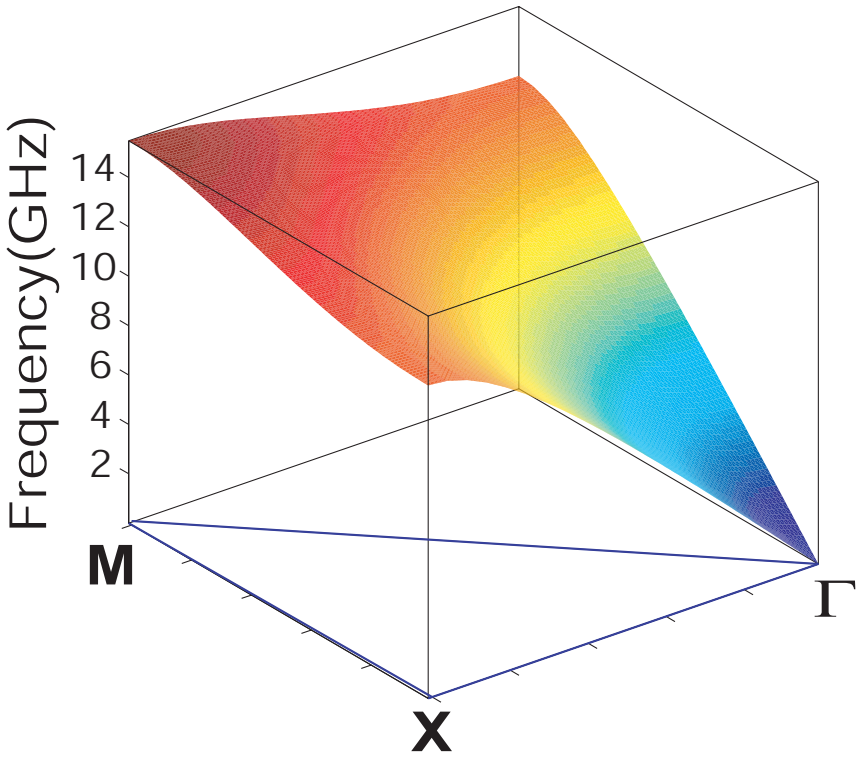

Figure 3.7: The valence band of our photonic crystal calculated within the first Brillouin zone. Using this two dimensional dispersion relation we can calculate the equal frequency contours of the photonic crystal.

an alternative to left handed materials [29]. Recent experimental and theoretical works indicate that negative refraction phenomena in photonic crystals are possible in regimes of negative group velocity and negative effective index above the first band near the first Brillouin zone center Γ [30, 31, 32]. But since the operation frequency lies within the upper bands of the photonic crystal, we have multiple Bragg waves propagating inside the photonic crystal, and coupling to the Bloch modes gets more difficult. Luo *et al.* [33] demonstrated theoretically all-angle negative refraction effect that does not employ a negative effective index of refraction and involves photonic crystals. Throughout this thesis, we focus on the first band of our photonic crystal for the experimental and theoretical demonstration of single beam negative refraction in two dimensional photonic crystals. Our structure consists of a square array of dielectric rods in air, having a dielectric constant $\varepsilon = 9.61$, diameter $2r = 3.15$ mm, and length $l = 15$ cm.

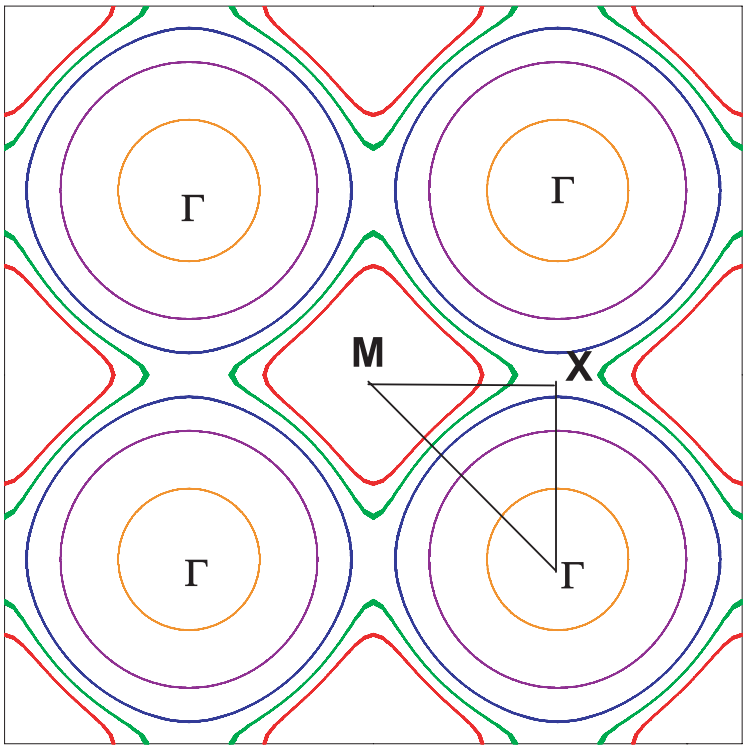

Figure 3.8: The equal frequency contours for the valence band of our photonic crystal in the extended Brillouin zone scheme. As can be seen here, the equal frequency contours are periodic in the momentum space.

Center to center separation between the rods is $a = 4.79$ mm. The transverse magnetic(TM) polarized band structure of our photonic crystal is shown in Fig. 3.6. As we have mentioned previously, we will focus on the first or the valence band of the photonic crystal. To study the refractive properties of the photonic crystal, we need to have the dispersion relation $\omega(k_x, k_y)$ of the valence band for every (k_x, k_y) lying within the first Brillouin zone. The two dimensional dispersion relation of the valence band calculated by plane wave expansion method, is shown in Fig. 3.7. As can be seen in Fig. 3.7 for low frequencies the photonic crystal acts like a regular dielectric medium since the dispersion relation resembles a cone. Thus the equal frequency contours are circular with positive gradient for low frequencies. This is consistent with the fact that for large wavelengths our crystal will act like an effective medium and can be modelled by the effective medium theory. However, as the frequency increases and gets close to the band edge, the dispersion relation becomes complicated along with the equal frequency

contours of our structure.

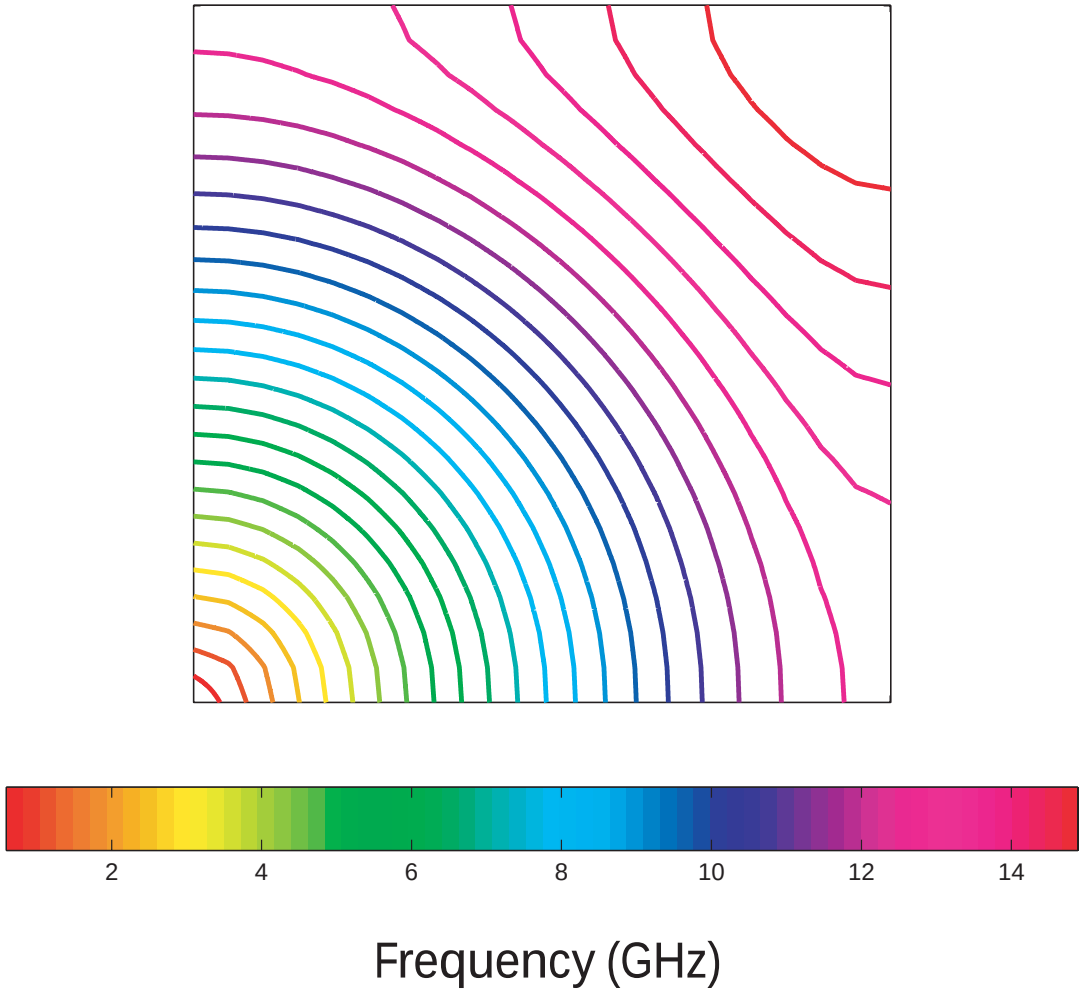

Figure 3.9: The equal frequency contours for the whole valence band of our photonic crystal in a quarter of the first Brillouin zone scheme. The equal frequency contours become anomalous as the frequency increases.

The equal frequency contours for the valence band of our photonic crystal in the extended Brillouin scheme is displayed in Fig. 3.8. As seen there, the equal frequency contours are periodic in the momentum space. This is similar to the case that we have for a grating. Since both structures are periodic in the real (coordinate) space, the structures exhibit periodic equal frequency contours in the indirect (momentum) space. We have also calculated the equal frequency contours in a quarter of the first Brillouin zone to analyze the structure better (Fig. 3.9). The equal frequency contours change from circular to square as the frequency

increases. This in turn enriches the refractive properties of our structure. For instance negative refraction is one of them. Following the analysis of Ref. [33], we have determined the negative refraction range for our structure. The frequency range that gives negative refraction extends from 13.1 GHz to 15.44 GHz, as shown in the shaded area of Fig. 3.6. To obtain negative refraction one needs to have the equal frequency contours for the photonic crystal that are both convex and larger than the equal frequency contours for air, which are circles with radii proportional to the frequency. The equal frequency contours for air and the photonic crystal at 13.698 GHz are shown in Fig. 3.10. Note that conservation of surface-parallel wave vector gives the direction of the refracted waves inside the photonic crystal (Fig. 3.10).

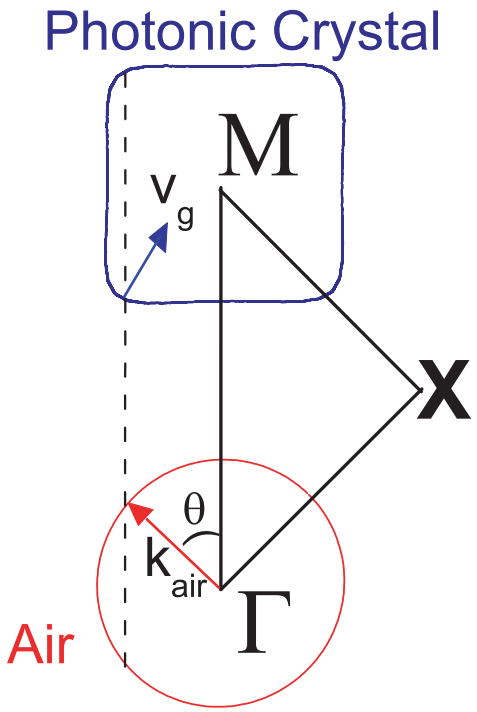

Figure 3.10: Equal frequency contours of air and our photonic crystal at 13.698 GHz. Here θ denotes the incidence angle from air to the photonic crystal. Note that conservation of surface-parallel wave vector gives the direction of the refracted waves inside the photonic crystal.

We performed transmission measurements for experimentally verifying the predicted negative refraction behavior in our structure. The experimental setup consists of an HP 8510C network analyzer, a microwave horn antenna as the

transmitter and a monopole antenna as the receiver (Fig. 3.11). The photonic crystal used in the refraction measurements has 17 layers in the propagation direction and 21 layers in the lateral direction. The interfaces are along ΓM direction. In all of our measurements and calculations the electric field is kept parallel to the rods. The horn antenna is oriented such that the incident waves make an angle of 45° with the normal of ΓM interface. We selected the operating frequency as 13.698 GHz.

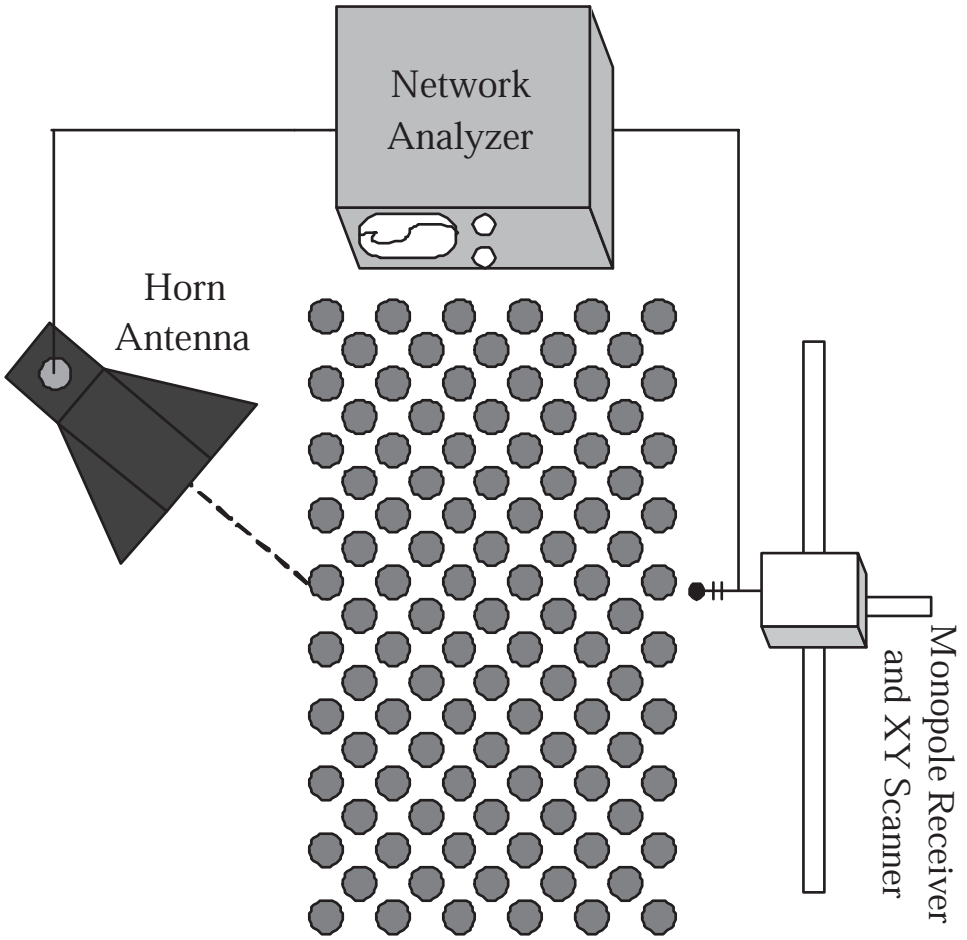

Figure 3.11: Experimental setup. For the refraction measurements a horn antenna is used as the transmitter, and a monopole antenna is used as a receiver.

As described later, at this frequency our structure exhibits the maximum angular range of negative refraction. To appreciate the difference between the negative and positive refraction, we propose a method where we scan the power distributions along the first interface and the second interface of the slab shaped

structure shown schematically in Fig. 3.12. We subsequently compare the peak positions of the power distributions along the two interfaces. If the center of the beam that emerges from the second interface is on the right-hand side of the center of the beam that is incident to the slab structure, we clearly have positive refraction. If the center of the beam that emerges from the second interface is on the left-hand side of the center of the beam that is incident to the slab structure, we apparently have negative refraction. This seems to be an amenable experiment to differ positive and negative refraction [34].

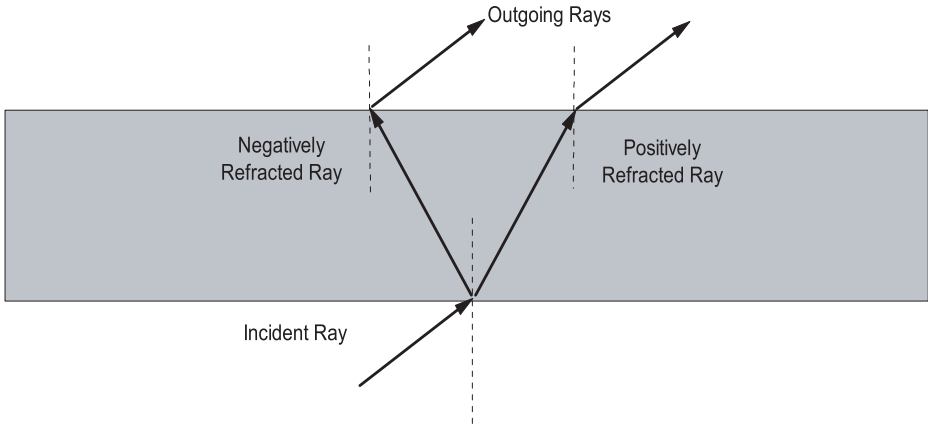

Figure 3.12: The schematics of the positive and the negative refraction.

We first removed the photonic crystal and measured the spatial power distribution along the air photonic crystal interface by scanning the receiver antenna, which corresponds to the incident power distribution. We then placed the photonic crystal and measured the spatial power distribution along the second(photonic crystal-air) interface. In our experiments we can only measure the power at a certain point, which corresponds to the time averaged intensity at that point. In order to make a realistic simulation of this structure, we calculated the spatial time averaged intensity distribution along the first interface without the photonic crystal and the spatial time averaged intensity distribution along the second interface in the vicinity of the photonic crystal by using the finite difference time domain method.

In the simulations the incident Gaussian beam width is selected to be 6 cm, which is equal to the width of the horn antenna used in the experiment. As shown in Fig. 3.13 the center of the outgoing Gaussian beam is shifted towards the left

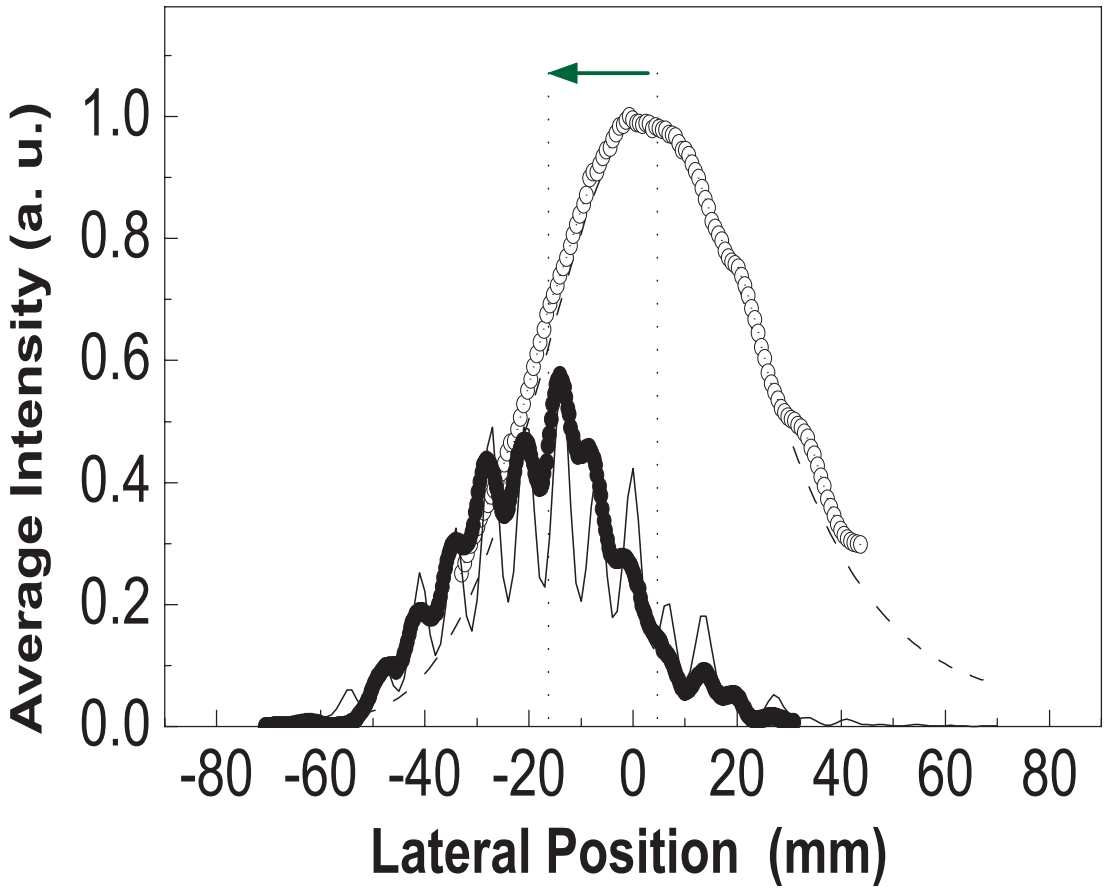

Figure 3.13: Negative refraction. Calculated average intensities at the second interface with (solid line) and at the first interface without the photonic crystal (dashed line). Measured power distributions at the second interface with $(-\bullet-)$ and at the first interface without the photonic crystal$(-\odot-)$.

hand side of the center of the incident Gaussian beam, which clearly corresponds to negative refraction. Since $\lambda > 2\sqrt{2}a$, Bragg reflections do not occur and only a single propagating beam is excited in the photonic crystal. For this reason we can still apply Snell's law in the following way

$$n(f, \mathbf{k_i}) \sin\theta_r = n_{air} \sin\theta_i, \tag{3.7}$$

where θ_i is the angle of incidence and θ_r is the angle of refraction inside the photonic crystal. Negative index of refraction determined from the experiment is -1.94, which is very close to the theoretical value of -2.06 calculated by the FDTD method. For comparison purposes, the measurements and the simulations

are repeated with a slab that contains only polystrene pellets, which has a refractive index of 1.46. As can be seen in Fig. 3.14, the refracted beam is now on the right hand side of the incident beam corresponding to a positive index of 1.52. To our knowledge, this is the first experimental demonstration of negative refraction in the valence band of a photonic crystal. The advantage of the first band is that we do not suffer from Bragg reflections that take place inside the photonic crystal and we have a well defined single beam propagation that is negatively refracted. Another advantage of operating in the valence band is that we have 63% transmission at this frequency. This is almost 3 orders of magnitude larger than the typical transmission in a left handed material [26, 35].

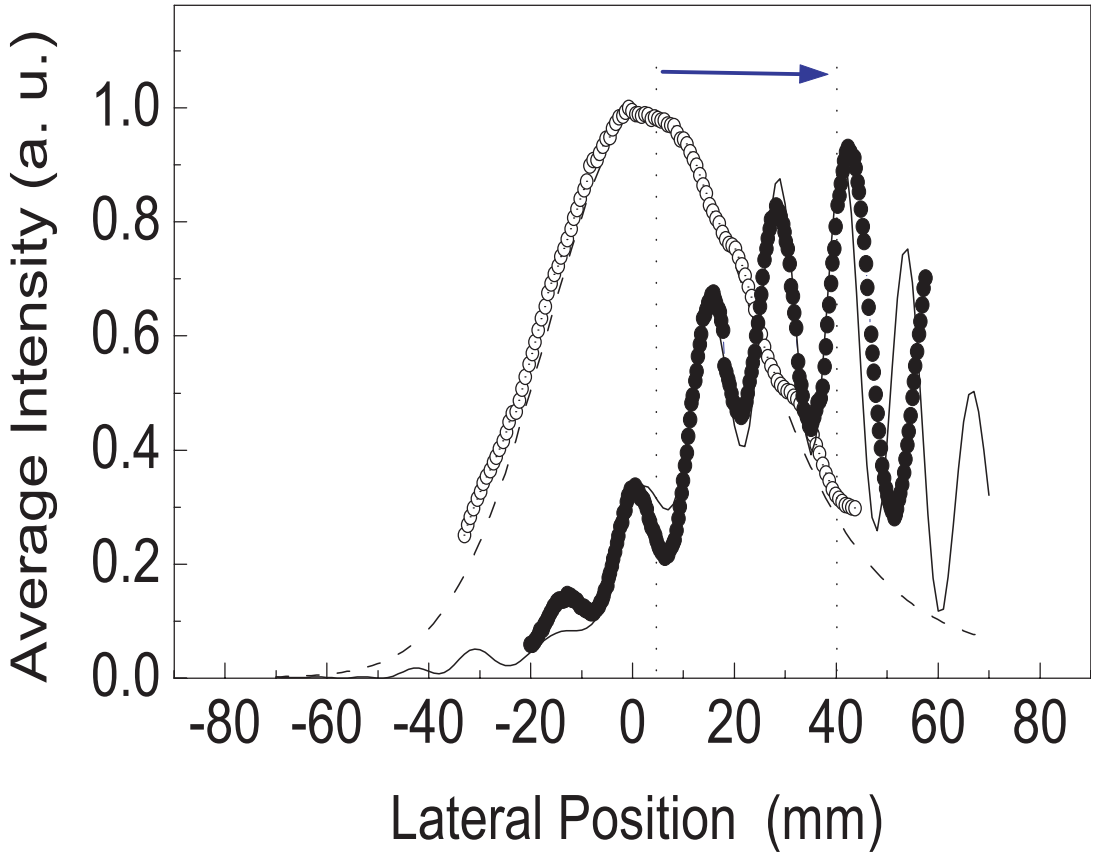

Figure 3.14: Positive refraction. Calculated average intensities at the second interface with (solid line) and at the first interface without the slab (dashed line). Measured power distributions at the second interface with $(- \bullet -)$ and at the first interface without the slab $(- \odot -)$.

In the aforementioned frequency range the equal frequency contours are square

shaped around the M point in the Brillouin zone (Fig. 3.10). This results in anisotropy for $n(f, \mathbf{k_i})$, where one expects to have different values for refractive index along different propagation directions. To demonstrate this anisotropy, the refractive index of the photonic crystal for certain angles of incidence at $f = 13.698$ GHz are measured. Figure 3.15 shows the angles of refraction for the experimental measurements and the FDTD simulations, where we observe a negative refraction behaviour for the incidence angles $> 20°$. In this angular range $\mathbf{v_g} \cdot \mathbf{k_{i\parallel}} < 0$, (while $\mathbf{v_g} \cdot \mathbf{k_i} > 0$), where $\mathbf{v_g}$ is the group velocity inside the PC that is given as $\nabla_k \omega(\mathbf{k})$ and $\mathbf{k_{i\parallel}}$ is the component of wave vector, incident from air to the photonic crystal, which is parallel to the interface.

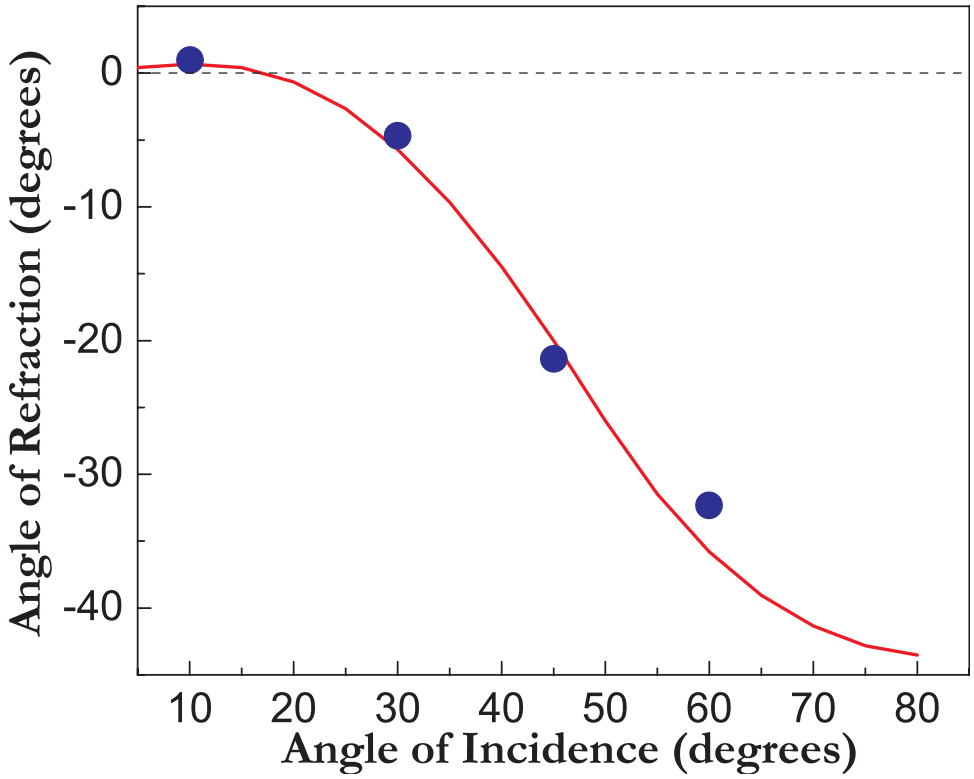

Figure 3.15: Comparison of measured(•) and calculated(solid line) angles of refraction versus angles of incidence at 13.698 GHz.

At 13.698 GHz, we achieve the maximum angular range of negative refraction for our structure. This frequency is the optimum value, because at this frequency the equal frequency contour for air has almost the same diameter with the equal frequency contour for the PC (Fig 3.10). If a higher frequency is used, the equal

frequency contour for air will be larger than the equal frequency contour for the PC. In such a case, the maximum angle where we obtain negative refraction gets smaller due to total internal reflection. This results in a narrower angle range for the negative refraction behavior. If a lower frequency is used, we then have equal frequency contour for air that is smaller than the equal frequency contour for the photonic crystal. This in turn increases the minimum angle where we obtain negative refraction, which again reduces the angle range for the negative refraction behavior.

Chapter 4

Superlensing and subwavelength resolution

The negative refraction that is not possible in ubiquitous materials has given birth to a novel class of applications. For instance, focusing of light by a slab structure with subwavelength resolution is achievable by these structures [25]. Lenses have been one of the prime tools of scientists for centuries. Their operation is well understood on the basis of classical optics: curved surfaces focus light by the virtue of the refractive index contrast (Fig. 4.1(b)). The limitations on the conventional lenses are determined by wave optics. Namely, no lens can focus light onto an area smaller than a square wavelength.

We can look more closely at the reason for the limitation in performance of a conventional lens. Let us consider an infinitesimal dipole of frequency ω in front of a lens. The electric field can be represented by the Fourier expansion,

$$\mathbf{E}(\mathbf{r},t) = \sum_{\sigma,\mathbf{k}} \mathbf{E}_\sigma(\mathbf{k}) e^{i\mathbf{k}\cdot\mathbf{r} - i\omega t} \ . \tag{4.1}$$

Here, the axis of the lens is chosen to be the z-axis. The dispersion relation for a linear medium tells us that,

$$k_z = +\sqrt{\omega^2/c^2 - k_x^2 - k_y^2}, \omega^2/c^2 > k_x^2 + k_y^2 \ , \tag{4.2}$$

The function of the lens is to apply a phase correction to each of the Fourier components so that at some distance beyond the lens the fields reassemble to a focus and an image of the dipole source appears. However, for larger values of the transverse wave vector,

$$k_z = +i\sqrt{k_x^2 + k_y^2 - \omega^2/c^2}, \omega^2/c^2 < k_x^2 + k_y^2 \, , \tag{4.3}$$

These evanescent waves decay exponentially with increasing z and no phase correction will restore them to their proper amplitude.

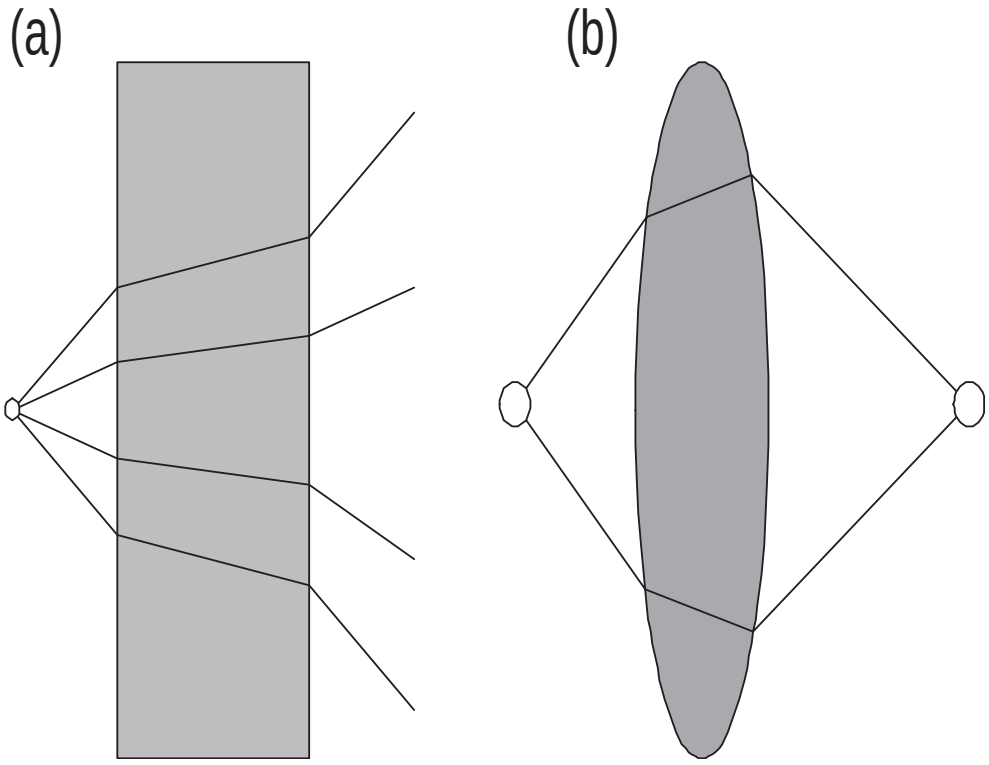

Figure 4.1: (a) The slab having a positive index of refraction. The rays emerging from the source diverge after passing through the slab. (b) A positive index lens. If we want to focus light and have an image as well, we need a lens that has curved surfaces.

They are effectively removed from the image which generally comprises only the propagating waves. Since the propagating waves are limited to,

$$k_x^2 + k_y^2 < \omega^2/c^2 \, , \tag{4.4}$$

the maximum resolution of the lens can never be greater than,

$$\Delta = \frac{2\pi}{k_{||}^{max}} = \frac{2\pi c}{\omega} = \lambda \ , \tag{4.5}$$

and this is true whatever the size of the aperture is. So, we can conclude that we can enhance the performance of a lens if we can somehow make this evanescent waves propagating inside the lens.

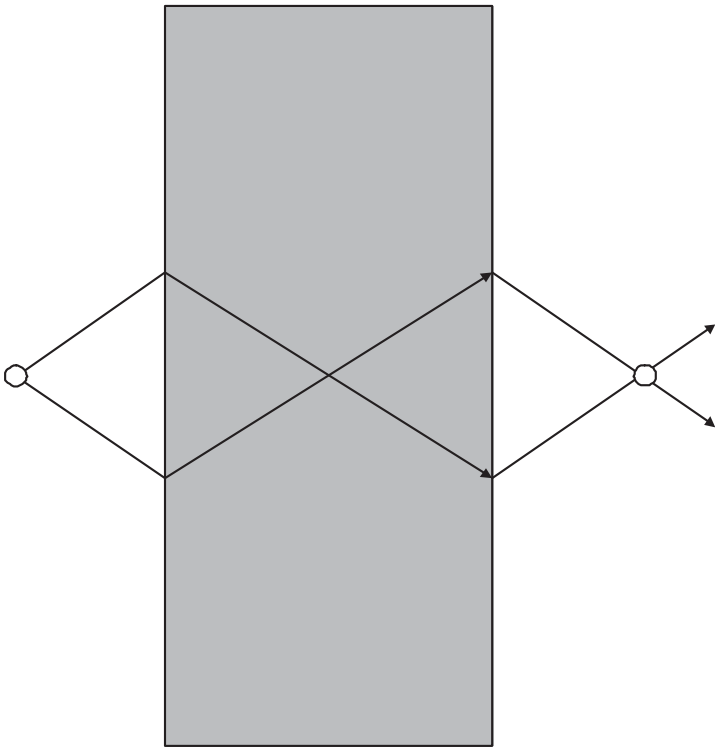

Figure 4.2: The slab having a negative index of refraction. The rays emerging from the source converge inside and after passing through the slab. If we want to focus light and have an image as well, we can use a slab having a negative index of refraction.

Meanwhile, we can demonstrate how a slab of negative refractive index can make a lens. First, we suppose that we have a slab of positive refractive index, and we place a point source in the vicinity of the lens. Since the lens has a positive index of refraction, the rays emerging from the source will diverge as seen in Fig. 4.1(a). And so the rays will never come into a focus beyond the slab in contrast to the focus in conventional lenses that have curved surfaces. The reason that the slab does not focus the rays is that we have positive refraction or

in other words the refracted beam is on the right-hand side of the normal. And after two refractions at the two interfaces the rays are shifted away from the axis of the slab rather than getting closer. If instead we have a slab that has a negative index of refraction, the refracted rays will be on the left-hand side of the interface normals. So, the rays will focus inside the lens as seen in Fig. 4.2. The rays will also experience negative refraction at the second interface. Subsequently, the light transmitted through the slab comes to a second focus beyond the slab. We are now aware of the interesting consequences of the negative refraction.

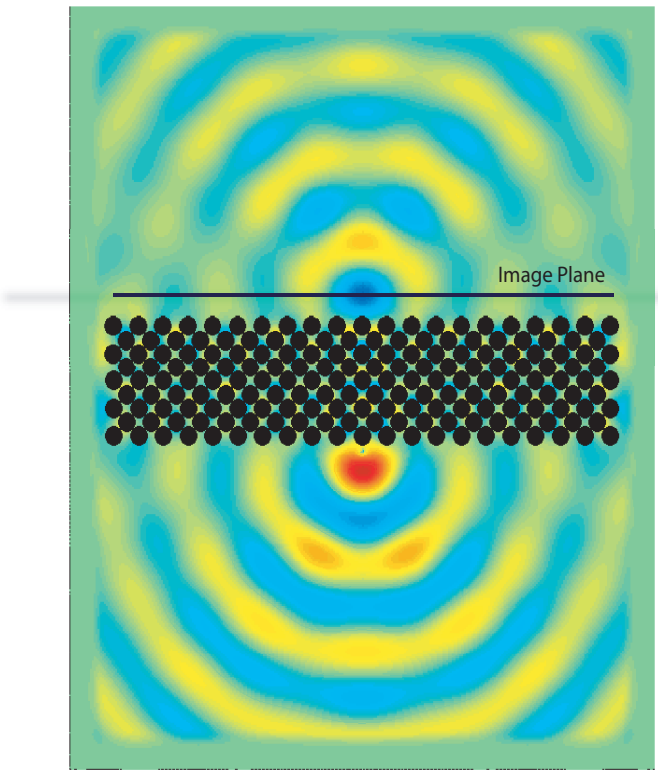

Figure 4.3: E_z field distribution of the source and the image in the vicinity of the photonic crystal. The image plane is also shown.

Since we have determined the optimum frequency for a broad angle negative refraction for our photonic crystal, we can use our crystal to test the superlensing effect that was predicted for negative refractive materials [25, 33, 36, 37]. In Fig. 4.3 we display the electric field distribution of our structure calculated by

finite difference time domain method. A point source is placed below our two-dimensional photonic crystal, and as can be seen in Fig. 4.3, the transmitted wave obviously come to a focus above the photonic crystal. For this purpose, a photonic crystal having 15 layers in the propagation direction and 21 layers in the lateral direction is used.

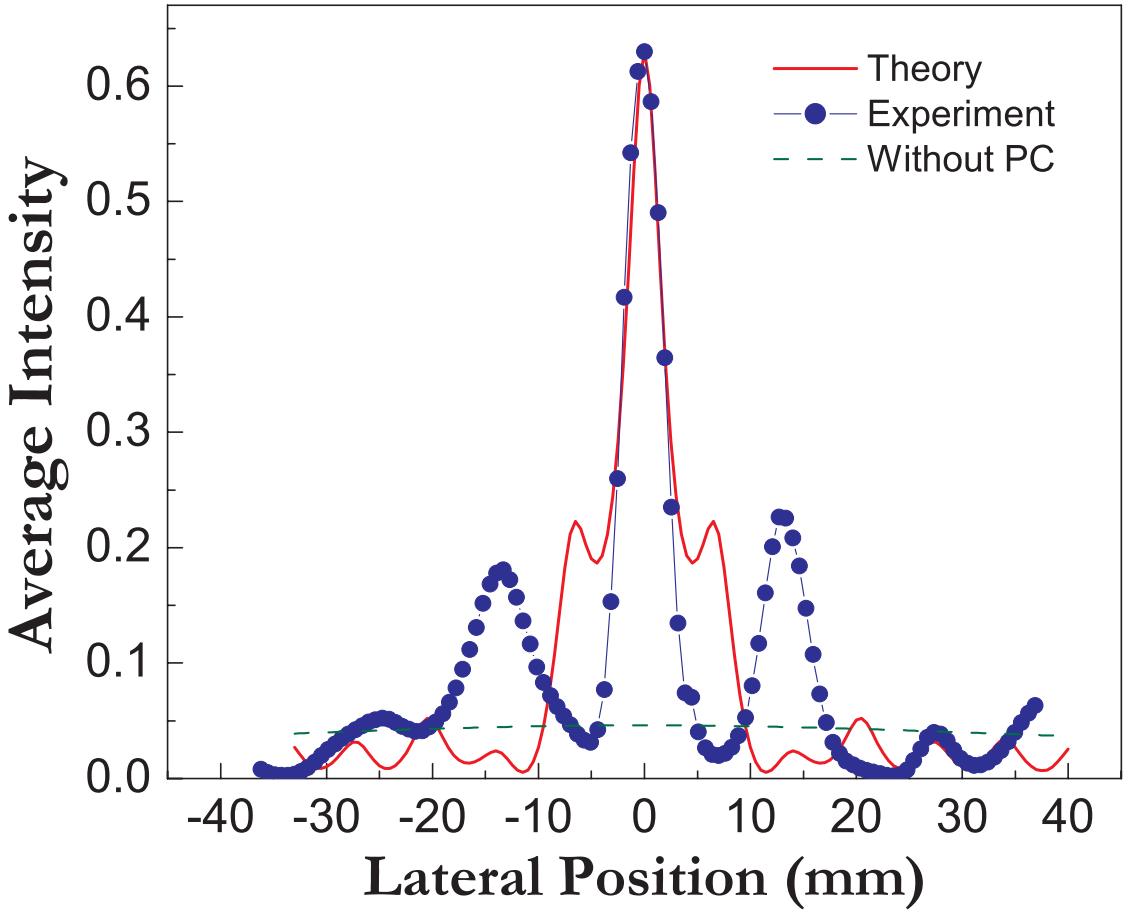

Figure 4.4: Measured power distribution (blue bullet) and calculated average intensity (solid line) at the image plane. Full width at half maximum of the measured image is 0.21λ . Spatial power distribution without PC is also shown (dashed line).

In our FDTD simulations, the surface of the photonic crystal is excited with a continuous wave point source that is placed at 0.7 mm away from the air-photonic crystal interface. An image of the source is formed at 0.7 mm away from the photonic crystal-air interface. To show the focusing on the image plane in the vicinity of the photonic crystal, the time averaged intensity distributions along

the image plane with and without the photonic crystal are calculated (Fig. 4.4). In the experiment, a monopole antenna is used as the point source (Fig. 4.5). The power distribution at the image plane is measured by scanning the transmission along the image plane. The measured distribution is also shown in Fig. 4.4.

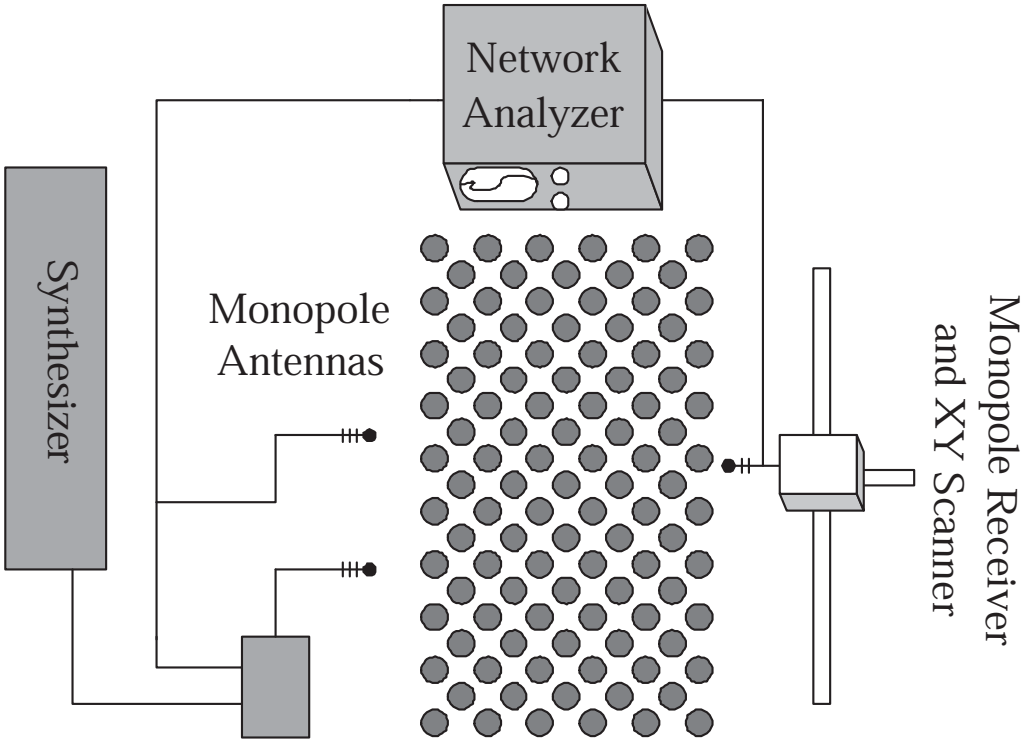

Figure 4.5: The experimental setup used both in the superlensing and subwavelength resolution measurements.

The full width half maximum (FWHM) of the measured focused beam is found to be 0.21λ , which is in good agreement with the calculated FWHM. The calculated FWHM of the beam at this plane without the photonic crystal is found to be 5.94λ . So, our structure exhibits $25\times$ focusing at this plane with respect to free space. However, in our structure superlensing effect can be observed only for a small separation between the point source and the photonic crystal. As the point source moves away from our finite-sized crystal, only a smaller portion of the electromagnetic waves become incident on the crystal within the negative refraction incidence angle range ($> 20^{\circ}$). So, as the separation between the source and the crystal increases, the superlensing effect gets weaker and it can not be observed for large separations.

Subwavelength resolution using negative refractive materials has been theoretically suggested [25]. As our structure exhibits negative refraction properties, we can also use our structure for this application. For this purpose, a crystal that consists of 15 layers in the propagation direction and 21 layers in the lateral direction is used. We place two point sources 0.7 mm away from the photonic crystal, which are separated by a distance $\lambda/3$ or 6.78 mm. Figure 4.6 shows the calculated power distribution at 0.7 mm away from the second interface with and without the photonic crystal. In the measurements the input power is split into two identical monopole antennas by a 3 dB splitter.

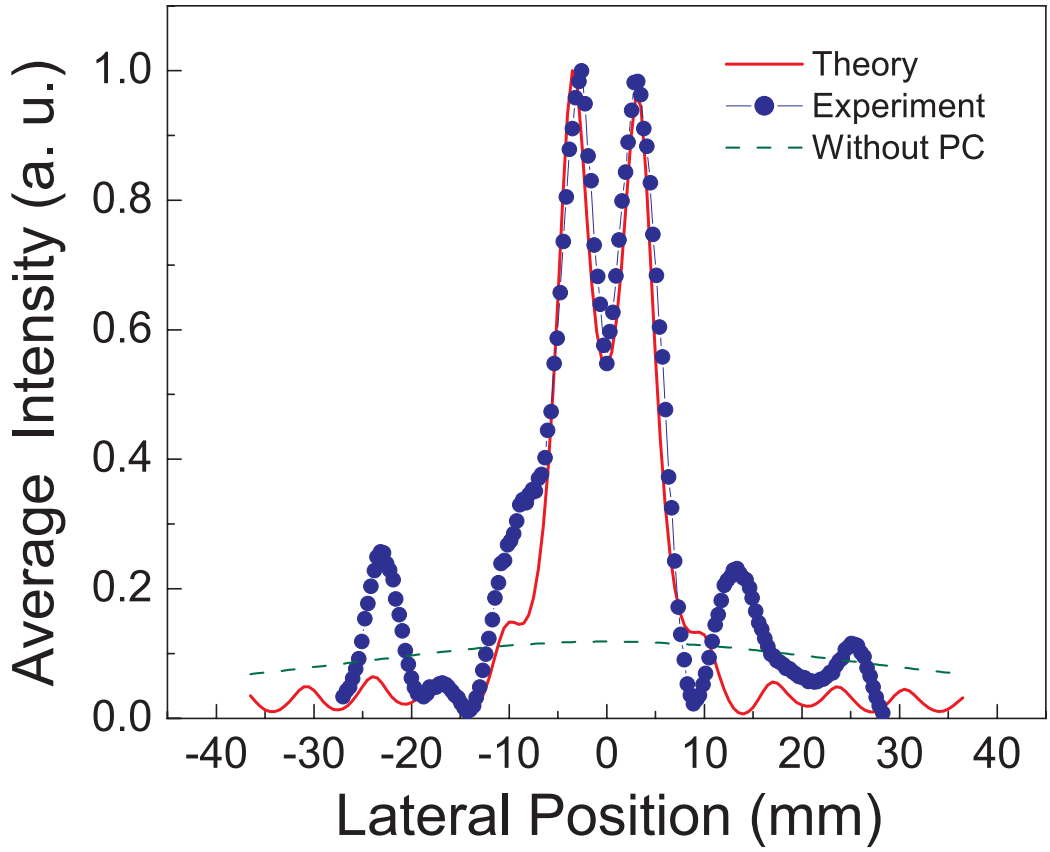

Figure 4.6: Measured power distribution (blue bullet) and calculated average intensity (solid line) at 0.7 mm away from the second interface. Calculated average intensity at this point without the photonic crystal is also shown (dashed line).

The measured power distribution at 0.7 mm away from the second interface is also plotted in Fig. 4.6. The peaks corresponding to each point source are clearly resolved in both measurement and simulation.

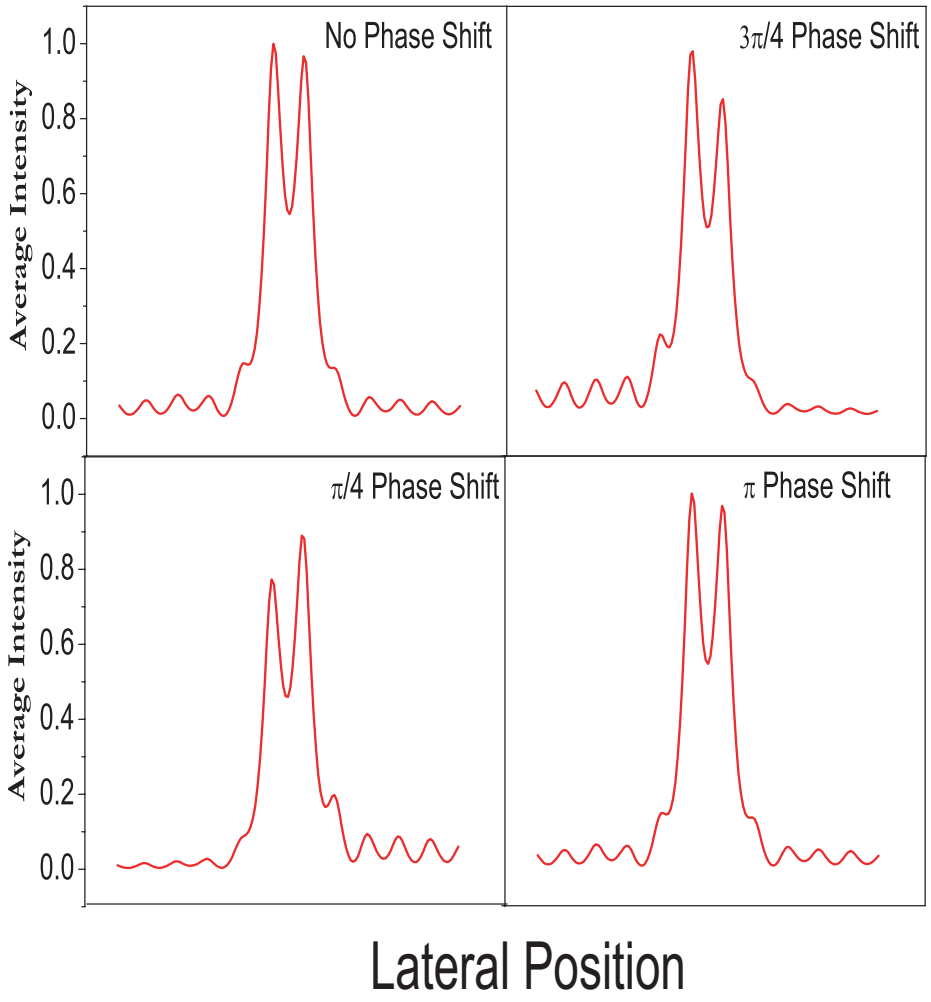

Figure 4.7: Calculated average intensity at 0.7 mm away from the second interface for various phase differences introduced between the point sources.

Since the point sources in the present experiments are obtained by splitting of the same signal, they remain coherent with respect to each other. Thus the obtained resolution may well be due to the interference effects. So, we checked how the performance of the lens will change if we introduce a phase difference between the two point sources. The best way to characterize the performance of the lens is simulating the structure rather than making an experiment since it will be very complicated to introduce a phase difference between the monopole antennas in the experiment. We have simulated the system for different phase differences. We can note that the peaks are still resolved in spite of the phase difference.

We have repeated the experiments and simulations with two incoherent point sources 0.7 mm away from the photonic crystal, which are separated by a distance of 6.78 mm and having frequencies 13.698 GHz and 13.608 GHz respectively. Figure 4.8 shows the calculated power distribution at 0.7 mm away from the second interface the PC. In the measurements two independent signal generators are used for driving the monopole antennas, and a powermeter is used for measuring the power distribution.

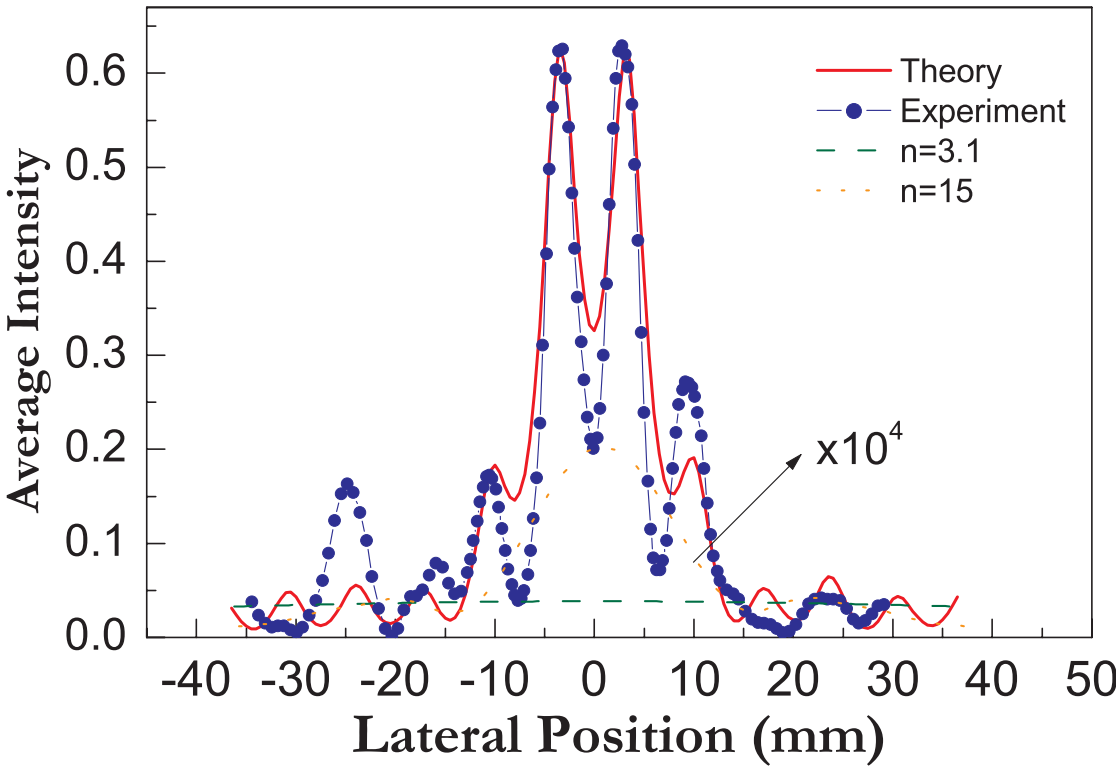

Figure 4.8: Measured power distribution (blue bullet) and calculated average intensity (solid line) at 0.7 mm away from the second interface for two incoherent sources. Calculated average intensity at this point without the photonic crystal is also shown (dashed line).

The measured power distribution at 0.7 mm away from the second interface is also plotted in Fig. 4.8. The peaks corresponding to each point source are clearly resolved in both measurement and simulation. To our knowledge, this is the first experimental observation of subwavelength resolution of two incoherent sources in negative refractive materials [38]. One can argue that the observed enhanced resolution can be just due to the large refractive index as in the case of oil (or solid)

immersion microscopy. In order to check this possibility, we repeat our incoherent source simulations using a dielectric slab with a high refractive index. Figure 4.8 shows the simulations made for $n = 3.1$ (refractive index of alumina) and $n = 15$. As can be seen from this figure, subwavelength resolution is not achieved even with a large index material. Besides, the large reflection resulting from the air-slab interface significantly reduces the transmitted power when compared to 63% transmission obtained from the PC at this operating frequency. So, even if the observed subwavelength resolution in our photonic crystal is a near field effect, this can not be achieved by ubiquitous materials. The negative refraction effect reported in this thesis depends only on the refractive index of the dielectric material and the geometrical parameters used in 2D photonic crystals. So, this effect can also be observed at optical wavelengths where it is possible to obtain similar refractive indices using transparent semiconductors. This is in contrast to the previously reported metal-based left-handed materials. In such structures, increased absorption in metals prohibits the scaling of these structures to the optical wavelengths. In terms of fabrication, a slab shaped lens structure is easier to fabricate than a conventional curved shaped lens structure. So, our slab shaped lens structure can also be used for nanophotonics and nanooptics applications.

Chapter 5

Conclusions

In this thesis work, we have investigated the negative refraction phenomenon in a two-dimensional photonic crystal, and subwavelength resolution in a photonic crsytal based superlens.

First, we examined the refractive properties of a two-dimensional dielectric photonic crystal. Strong frequency dependence of the refractive index of the photonic crystal is observed. We have in particular focused on possibility of negative refraction in these structures. To obtain the frequency range within which the negative refraction and the other peculiar properties incorporated with it, we have calculated the equal frequency contours of our photonic crystal with the photonic plane wave expansion method. We found out that 13.7 GHz is the optimum frequency for negative refraction. We took transmission measurements to confirm our structure's predicted negative refraction: we used the the interfaces of the photonic crystal in the $\Gamma - M$ direction. Our experiments were simulated with the finite-difference time-domain method. The negative index of refraction was determined to be -1.94, which is close to the theoretical value of -2.06 calculated by the finite-difference time-domain method.

The advantage of negative refraction in the valence band is that there is no Bragg reflection; such reflections occur in higher bands of the photonic crystal, and we have a well-defined, single-beam propagation that is negatively refracted.

Another advantage of operating in the valence band is that the transmission efficiency at this frequency is 63%, which is almost three orders of magnitude larger than the typical transmission efficiency in a left-handed material.

This experimental verification of negative refraction is a step towards the realization of a 'superlens' that will be able to focus features smaller than the wavelength of light. Since we know that we have a negative refractive material , we have furthered our investigation by using our crystal to test the superlensing effect that was predicted for negative refractive materials. We have demonstrated that the image of two coherent point sources separated by a distance of $\lambda/3$ can be resolved. We have extended our approach to the case with two incoherent point sources, and we have achieved subwavelength resolution for this configuration as well. The measurements are in good agreement with the finite-difference time-domain method simulations. To our knowledge, this is the first demonstration of subwavelength resolution of electromagnetic waves in a negative index material.

The negative refraction effect reported in this thesis depends only on the refractive index of the dielectric material and the geometrical parameters used in 2D photonic crystals. So, this effect can also be observed at optical wavelengths where it is possible to obtain similar refractive indices using transparent semiconductors. This is in contrast to the previously reported metal-based left-handed materials. In such structures, increased absorption in metals prohibits the scaling of these structures to the optical wavelengths. In terms of fabrication, a slab shaped lens structure is easier to fabricate than a conventional curved shaped lens structure. So, our slab shaped lens structure can also be used for nanophotonics and nanooptics applications.

As future work, we are planning to build structures that exhibit all-angle negative refraction (having a circular equal frequency contour with negative gradient), and that operate at higher frequencies for instance in the milimeter and optical wave regimes. We have preliminary results that a metallic photonic crystal in which just the dielectric rods are changed with metallic ones will exhibit all-angle negative refraction and subwavelength focusing as well. For the dielectric case operating at higher frequencies, we are planning to fabricate them by

micro-machining techniques. And the dielectric structure operating at the optical wavelengths can be fabricated by using electron beam lithography and deep reactive ion etching techniques.

Bibliography

[1] C. Kittel, *Introduction to Solid State Physics*, p. 75, John Wiley and Sons, New York, 7^{th} edition edition, 1996.

[2] E. Yablonovitch, "Inhibited spontaneous emission in solid-state physics and electronics," *Phys. Rev. Lett.*, vol. 58, pp. 2059–2062, 1987.

[3] S. John, "Strong localization of photons in certain disordered dielectric superlattices," *Phys. Rev. Lett.*, vol. 58, pp. 2486–2489, 1987.

[4] E. Yablonovitch, T. J. Gmitter, R. D. Meade, A. M. Rappe, K. D. Brommer, and J. D. Joannopoulos, "Donor and acceptor modes in photonic band structure," *Phys. Rev. Lett.*, vol. 67, pp. 3380–3383, 1991.

[5] K. M. Ho, C. T. Chan, C. M. Soukoulis, R. Biswas, and M. M. Sigalas, "Photonic band gaps in three dimensions: New layer-by-layer periodic structures," *Solid State Commun.*, vol. 89, pp. 413, 1994.

[6] E. Ozbay, E. Michel, G. Tuttle, R. Biswas, K.M. Ho, J. Bostak, and D. M. Bloom, "Terahertz spectroscopy of three-dimensional photonic band gap crystal," *Opt. Lett.*, vol. 19, pp. 1155–1157, 1994.

[7] E. Ozbay, "Layer-by-layer photonic crystals from microwave to far-infrared frequencies," *J. Opt. Soc. Am. B*, vol. 13, pp. 1945–1955, 1996.

[8] S. Y. Lin, J. G. Fleming, D. L. Hetherington, B. K. Smith, R. Biswas, K. M. Ho, M. M. Sigalas, W. Zubrzycki, S. R. Kurtz, and J. Bur, "A three-dimensional photonic crystal operating at infrared wavelength," *Nature (London)*, vol. 394, pp. 251–253, 1998.

[9] J. G. Fleming and Shawn-Yu Lin, "Three-dimensional photonic crystal with a stop band from 1.35 to 1.95 μm," *Opt. Lett.*, vol. 24, pp. 49–51, 1999.

[10] S. Noda, A. Chutinan, and M. Imada, "Trapping and emission of photons by a single defect in a photonic bandgap structure," *Nature*, vol. 407, pp. 608–610, 2000.

[11] A. Mekis, J. C. Chen, I. Kurland, S. Fan, P. R. Villeneuve, and J. D. Joannapoulos, "High transmission through sharp bends in photonic crystal waveguides," *Phys. Rev. Lett.*, vol. 77, pp. 3787–3790, 1996.

[12] S. Y. Lin, E. Chow, V. Hietala, P. R. Villeneuve, and J. D. Joannopoulos, "Experimental demonstration of guiding and bending of electromagnetic waves in a photonic crystal," *Science*, vol. 282, pp. 274–276, 1998.

[13] M. Bayindir, B. Temelkuran, and E. Ozbay, "Tight-binding description of the coupled defect modes in three-dimensional photonic crystals," *Phys. Rev. Lett.*, vol. 84, pp. 2140–2143, 2000.

[14] M. Bayindir, B. Temelkuran, and E. Ozbay, "Propagation of photons by hopping: A waveguiding mechanism through localized coupled-cavities in three-dimensional photonic crystals," *Phys. Rev. B*, vol. 61, pp. R11855–R11858, 2000.

[15] M. Bayindir and E. Ozbay, "Heavy photons at coupled-cavity waveguide band edges in a three-dimensional photonic crystal," *Phys. Rev. B*, vol. 62, pp. R2247–R2250, 2000.

[16] J. D. Jackson, *Classical Electrodynamics*, John Wiley and Sons, New York, NY, 1962.

[17] N. Bloembergen, *Nonlinear Optics*, W. A. Benjamin, New York, NY, 1965.

[18] J. D. Joannopoulos, R. D. Meade, and J. N. Winn, *Photonic Crystals: Molding the Flow of Light*, Princeton University Press, Princeton, NJ, 1995.

[19] R. Shankar, *Principles of Quantum Mechanics*, Plenum Press, New York, NY, 1982.

[20] J. J. Sakurai, *Modern Quantum Mechanics*, Addison-Wesley, Reading, MA, 1985.

[21] K. M. Leung and Y. F. Liu, "Full vector wave calculation of photonic band structures in face-centered-cubic dielectric media," *Phys. Rev. Lett.*, vol. 65, pp. 2646–2649, 1990.

[22] Z. Zhang and S. Satpathy, "Electromagnetic wave propagation in periodic structures: Bloch wave solution of maxwell's equations," *Phys. Rev. Lett.*, vol. 65, pp. 2650–2653, 1990.

[23] K. Sakoda, *Optical Properties of Photonic Crystals*, Springer-Verlag, Berlin Heidelberg New York, 2001.

[24] V. G. Veselago, "The electrodynamics of substances with simultaneously negative values of ε and μ," *Sov. Phys. Usp.*, vol. 92, pp. 509, 1968.

[25] J. B. Pendry, "Negative refraction makes a perfect lens," *Phys. Rev. Lett.*, vol. 85, pp. 3966–3969, 2000.

[26] D. C. View S. C. Nemat-Nasser D. R. Smith, W. J. Padilla and S. Schultz, "Composite medium with simultaneously negative permeability and permittivity," *Phys. Rev. Lett.*, vol. 84, pp. 4184–4187, 2000.

[27] S. C. Nemat-Nasser R. A. Shelby, D. R. Smith and S. Schultz, "Microwave transmission through a two-dimensional, isotropic, left-handed metamaterial," *Appl. Phys. Lett.*, vol. 78, pp. 489–491, 2001.

[28] D. J. Robbins J. B. Pendry, A. J. Holden and W. J. Stewart, "Magnetism from conductors and enhanced nonlinear phenomena," *IEEE Trans. Microwave Theory Tech.*, vol. 47, pp. 2075–2084, 1999.

[29] D. R. Smith R. A. Shelby and S. Schultz, "Experimental verification of a negative index of refraction.," *Science*, vol. 292, pp. 77–79, 2001.

[30] M. Notomi, "Theory of light propagation in strongly modulated photonic crystals: Refractionlike behavior in the vicinity of the photonic band gap," *Phys. Rev. B*, vol. 62, pp. 10696–10705, 2000.

[31] S. Enoch B. Gralak and G. Tayeb, "Theory of light propagation in strongly modulated photonic crystals: Refractionlike behavior in the vicinity of the photonic band gap," *J. Opt. Soc. Am. A*, vol. 17, pp. 1012–1020, 2000.

[32] A. Tomita M. Notomi T. Tamamura T. Sato H. Kosaka, T. Kawashima and S. Kawakami, "Superprism phenomena in photonic crystals," *Phys. Rev. B*, vol. 58, pp. R10096–R10099, 1998.

[33] J. D. Joannopoulos J. B. Pendry C. Luo, S. G. Johnson, "All-angle negative refraction without negative effective index," *Phys. Rev. B*, vol. 65, pp. 201104, 2002.

[34] E. Ozbay S. Foteinopoulou E. Cubukcu, K. Aydin and C. M. Soukoulis, "Negative refraction by photonic crystals," *Nature*, vol. 423, pp. 604–605, 2003.

[35] E. Ozbay P. Markos M. Bayindir, K. Aydin and C. M. Soukoulis, "Transmission properties of composite metamaterials in free space," *Appl. Phys. Lett.*, vol. 81, pp. 120–122, 2002.

[36] R. W. Ziolkowski and E. Heyman, "Wave propagation in media having negative permittivity and permeability," *Phys. Rev. E*, vol. 64, pp. 056625, 2001.

[37] J. B. Brock A. A. Houck and I. L. Chuang, "Transmission properties of composite metamaterials in free space," *Phys. Rev. Lett.*, vol. 90, pp. 137401, 2002.

[38] E. Ozbay S. Foteinopoulou E. Cubukcu, K. Aydin and C. M. Soukoulis, "Subwavelength resolution in a two-dimensional photonic crystal based superlens," *Submitted to Phys. Rev. Lett.*, 2003.